

# **Lecithin:Retinol Acyl Transferase (LRAT) induces the formation of lipid droplets**

Martijn R. Molenaar<sup>§</sup>, Tsjerk A. Wassenaar<sup>‡</sup>, Kamlesh K. Yadav<sup>#</sup>, Alexandre Toulmay<sup>#</sup>, Muriel C. Mari<sup>&</sup>, Lucie Caillon<sup>£</sup>, Aymeric Chorlay<sup>£</sup>, Maya W. Haaker<sup>§</sup>, Richard W. Wubbolts<sup>§</sup>, Martin Houweling<sup>§</sup>, A. Bas Vaandrager<sup>§</sup>, Fulvio Reggiori<sup>&</sup>, Abdou Rachid Thiam<sup>£</sup>, William A. Prinz<sup>#</sup>, J. Bernd Helms<sup>§\*</sup>

<sup>§</sup> Department of Biochemistry and Cell Biology, Faculty of Veterinary Medicine, Utrecht University, 3584 CM, Utrecht, The Netherlands

<sup>‡</sup> Groningen Biomolecular Sciences and Biotechnology Institute and Zernike Institute for Advanced Materials, University of Groningen, Nijenborgh 7, 9747 AG Groningen, The Netherlands

<sup>#</sup> National Institute of Diabetes and Digestive and Kidney Diseases, NIH, Bethesda, MD 20892, USA

<sup>&</sup> Department of Cell Biology, University of Groningen, University Medical Center Groningen, Groningen, Netherlands

<sup>£</sup> Laboratoire de Physique Statistique, Ecole Normale Supérieure, PSL Research University, Sorbonne Université, UPMC Université Paris 06, Université Paris Diderot, CNRS, Paris, France.

\* To whom correspondence should be addressed: J.B.H ([J.B.Helms@uu.nl](mailto:J.B.Helms@uu.nl))

1 **Abstract**

2

3 Lipid droplets are unique and nearly ubiquitous organelles that store neutral lipids in a  
4 hydrophobic core, surrounded by a monolayer of phospholipids. The primary neutral  
5 lipids are triacylglycerols and steryl esters. It is not known whether other classes of  
6 neutral lipids can form lipid droplets by themselves. Here we show that production of  
7 retinyl esters by lecithin:retinol acyl transferase (LRAT) in yeast cells, incapable of  
8 producing triacylglycerols and steryl esters, causes the formation of lipid droplets. By  
9 electron microscopy, these lipid droplets are morphologically indistinguishable from  
10 those in wild-type cells. *In silico* and *in vitro* experiments confirmed the propensity of  
11 retinyl esters to segregate from membranes and to form lipid droplets. The hydrophobic  
12 N-terminus of LRAT displays preferential interactions with retinyl esters in membranes  
13 and promotes the formation of large retinyl ester-containing lipid droplets in mammalian  
14 cells. Our combined data indicate that the molecular design of LRAT is optimally suited  
15 to allow the formation of characteristic large lipid droplets in retinyl ester-storing cells.

16

17 **Keywords**

18

19 LRAT; vitamin A; retinol; retinyl ester; retinoids; lipid droplets; lipid droplet size;  
20 nucleation; lipid:protein interaction; hepatic stellate cells; liver

## 21 Introduction

22

23 Lipid droplets (LDs) form a ubiquitous class of organelles, best known for their role as  
24 storage of neutral lipids for a multitude of functions such as creating an energy reservoir,  
25 a source for building blocks, protection against lipotoxicity, a role in cell cycle, and  
26 storage of signaling lipids (Hashemi and Goodman, 2015; Pol et al., 2014; Thiam and  
27 Beller, 2017; Walther and Farese, 2012). However, LDs also play important roles in lipid  
28 metabolism and homeostasis. Dysfunction of LD synthesis has been linked to a range of  
29 diseases. The physiological role of LDs thus appears significantly larger than considered  
30 previously (Krahmer et al., 2013; Welte, 2015).

31 LDs have a unique organellar architecture with a lipid monolayer surrounding a  
32 hydrophobic core that consists of neutral lipids. A number of specific proteins associate  
33 with LDs regulating organelle and lipid dynamics. Recent advances have started to shed  
34 light on the mechanism of LD biogenesis. In the most prevalent view, LD formation is  
35 primarily driven by triacylglycerol (TAG) synthesis at the endoplasmic reticulum (ER).  
36 TAG accumulates at the interphase of the ER bilayer, until a critical demixing  
37 concentration is reached and phase separation occurs, leading to lens formation and  
38 membrane deformation (Thiam and Forêt, 2016; Walther et al., 2017). During this  
39 process of nucleation, neutral lipids coalesce to form lenses between the two leaflets of  
40 the membrane bilayer. Indeed, lenses of about 50nm have been observed in the ER upon  
41 induction of LD formation in yeast (Choudhary et al., 2015). As neutral lipid synthesis  
42 continues, nascent LDs may bud from the endoplasmic reticulum. Although this process  
43 may not require proteins other than TAG synthesizing enzymes such as DGAT 1/2 and  
44 ACSL3 (Kassan et al., 2013; Pol et al., 2014; Thiam and Forêt, 2016; Walther et al.,  
45 2017), several proteins and lipids have been identified in the regulation of LD number  
46 and size as well as LD dynamics.

47

48 The abundant presence of large LDs is a hallmark of hepatic stellate cells (HSCs) in  
49 normal liver. HSCs are specialized in the storage of retinol (vitamin A) as retinyl esters,  
50 giving the LDs their characteristic autofluorescent properties. After liver injury, the fine  
51 structure of HSCs changes considerably. They lose their characteristic LDs and  
52 transdifferentiate into myofibroblasts, in preparation to secrete collagen (Blaner et al.,  
53 2009; Friedman, 2008). Lipidomic analysis revealed complex dynamics of disappearance  
54 of different classes of neutral lipids during HSC activation (Testerink et al., 2012). Recent  
55 research shows the presence of two different types of LDs, so-called preexisting “original”  
56 LDs with relatively slow turnover and rapidly “recycling” LDs that transiently appear  
57 during activation of HSCs (Ajat et al., 2017; Molenaar et al., 2017; Tuohetahuntala et al.,  
58 2016). Whereas synthesis and breakdown of TAGs in rapidly recycling LDs is mediated  
59 by DGAT1 and ATGL (Tuohetahuntala et al., 2016), less is known about the turnover of  
60 preexisting LDs. Lysosomes play an important role in the degradation of these LDs  
61 (Tuohetahuntala et al., 2017) and this is likely to be related to the observed importance of  
62 the autophagic pathway in HSC activation (Hernandez-Gea and Friedman, 2011; Thoen et  
63 al., 2011).

64

65 Surprisingly, inhibition of DGAT1 does not affect the dynamics of the preexisting LDs  
66 nor does it affect the synthesis of retinyl esters in isolated primary HSCs (Ajat et al., 2017;

67 [Tuohetahuntala et al., 2016](#)). However, HSCs contain a specialized enzyme called  
68 lecithin:retinol acyltransferase (LRAT) that catalyzes a trans-esterification reaction  
69 between the *sn-1* position of phosphatidylcholine (PC) and all-*trans*-retinol to form  
70 all-*trans*-retinyl ester ([Fig. 1A,B](#)) ([Goleczak et al., 2012](#); [Ruiz and Bok, 2010](#)). As LRAT is  
71 the main contributor to retinyl ester storage in the liver ([Liu and Gudas, 2005](#); [O'Byrne et](#)  
72 [al., 2005](#)), we investigated the possibility that LRAT-mediated retinyl ester synthesis  
73 drives the generation of the relatively large, retinyl ester-containing LDs in quiescent  
74 HSCs.  
75

## 76 Results

77

### 78 LRAT expression generates UV-positive lipid droplets

79 Primary and quiescent HSCs spontaneously transdifferentiate into activated HSCs  
80 (myofibroblasts) *ex vivo* upon isolation and subsequent culture, resulting in LD  
81 disappearance. Quiescent and activated HSCs can be identified based on their high  
82 expression of desmin, whereas these two HSC populations can be distinguished from  
83 each other by an increased alpha smooth muscle actin ( $\alpha$ -SMA) expression in activated  
84 HSCs (Blaner et al., 2009; Friedman, 2008) (Fig. 1C,D). In addition, LRAT expression  
85 decreases (Blaner et al., 2009; Kluwe et al., 2011) (Fig. 1E). We previously presented  
86 evidence for neutral lipid dynamics during HSC activation that is consistent with the  
87 existence of two different pools of LDs (Molenaar et al., 2017; Tuohetahunttila et al.,  
88 2017). To visualize these two different pools, we made use of the autofluorescent  
89 properties of retinyl esters in preexisting “original” LDs that are a hallmark of quiescent  
90 HSCs (Ajat et al., 2017; Friedman, 2008). After fixation of freshly isolated HSCs, retinyl  
91 esters (UV autofluorescence) and LDs (LD540) were imaged by confocal microscopy. We  
92 observed two distinct populations of LDs: large UV<sup>+</sup>LD540<sup>+</sup> structures containing high  
93 amounts of REs and UV<sup>-</sup>LD540<sup>+</sup> structures - depleted from REs - with smaller diameters  
94 (Fig. 1F). These observations are also in good agreement with our recent findings that  
95 LDs in LRAT<sup>-/-</sup> HSCs were significantly smaller as compared to LDs from wild-type cells  
96 (Ajat et al., 2017). Together, these data suggest a role for LRAT in the formation of  
97 distinct vitamin A-containing LDs that are a hallmark of hepatic stellate cells (HSCs).

98

99 To understand the role of LRAT in LD biology, we stably transfected CHO-k1 cells with  
100 a plasmid carrying LRAT-GFP. Lipidomic analysis of CHO cells expressing LRAT  
101 showed that retinyl ester synthesis was observed only after addition of retinol (ROH) as  
102 substrate to the medium (Fig. 1G (UV<sup>+</sup>LDs) and Suppl. Fig. 1A) and revealed the  
103 presence of predominantly saturated (16:0 and 18:0) and mono-unsaturated (18:1) fatty  
104 acids (Suppl. Fig. 1A). This composition reflects the catalytic activity of LRAT, using  
105 fatty acids at the *sn*-1 moiety of PC for esterification (Golczak et al., 2012; MacDonald  
106 and Ong, 1988). CHO cells do not contain detectable amounts of enzymatic activity of  
107 LRAT (Suppl. Fig. 1B) and in the absence of LRAT they can synthesize retinyl esters  
108 using a different mechanism involving DGAT1 (Ajat et al., 2017; Orland et al., 2005).  
109 This reaction occurs with much lower efficiency and results in a different species profile  
110 of retinyl esters (Suppl. Fig. 1C). Inhibition of DGAT1 activity in CHO-k1 cells  
111 expressing LRAT-GFP showed no inhibition of retinyl ester synthesis, which confirms  
112 that LRAT is the primary retinyl ester synthesizing enzyme (Suppl. Fig. 1D). Both  
113 CHO-k1 cells expressing GFP or LRAT-GFP showed increased LD540 fluorescence after  
114 incubation with oleic acid (OA). However, only LRAT-GFP expressing cells showed an  
115 increase in LDs after incubation with ROH, confirming the ability of LRAT to esterify  
116 ROH (Fig. 1G). Furthermore, these LDs exhibited UV-autofluorescence and were larger  
117 in diameter as compared to OA-stimulated LDs, which in turn were not autofluorescent  
118 (Fig. 1H). Similar results were obtained after transfection of human HSC-derived cell line  
119 LX-2 with LRAT (Suppl. Fig. 2). To exclude the possibility that the observed large  
120 UV<sup>+</sup>LDs were in fact clusters of small LDs that could not be distinguished due to the  
121 limited resolution of conventional confocal microscopy, we also imaged both conditions

122 by super resolution microscopy (3D structured illumination microscopy, 3D-SIM). Using  
123 SIM, we observed both small and large sized LDs in LRAT-dependent LD-synthesis and  
124 with a clustered appearance (Fig. 1I). In the presence of OA, the LDs displayed a more  
125 homogeneous size-distribution of relative small LDs and a ‘dispersed’ localization  
126 through the cell (Fig. 1I, Suppl. Video 1-2).

127

### 128 **LRAT-mediated LD formation is independent of TAG synthesis.**

129 TAG synthesis is a driving force in LD biogenesis. The last step in TAG synthesis is  
130 performed by DGAT1 or DGAT2, enzymes that transfer activated fatty acids to  
131 diacylglycerol. Fatty acid activation is performed by acyl-CoA synthetases and their  
132 knockdown or pharmaceutical inhibition after OA-stimulation led to a decreased number  
133 of (pre-)LDs (Kassan et al., 2013). Acyl-CoA is, however, not involved in the  
134 transesterification reaction of a fatty acid from PC to ROH by LRAT to generate retinyl  
135 esters. To determine whether LRAT requires TAG synthesis for retinyl ester synthesis and  
136 formation of RE-containing LDs, we pre-incubated LRAT-GFP expressing cells under  
137 low serum conditions overnight and subsequently incubated the cells in the presence of  
138 triacsin C, a drug that inhibits acyl-CoA synthesizing activities (Igal et al., 1997). In the  
139 presence of triacsin C, the number of LDs was strongly reduced, both in the presence and  
140 absence of OA (Fig. 2A). In the presence of ROH, however, formation of large LDs was  
141 still observed. These results confirm that LRAT does not depend on the presence of  
142 acyl-CoA and supports the possibility that LD-formation via LRAT has a distinct  
143 mechanism that is independent of TAG (DGAT/ACSL-mediated) LD formation.

144

145 Some LDs could still be observed in cells treated with triacsin C and therefore we could  
146 not exclude the possibility that, rather than TAG synthesis, TAG-filled LDs are required  
147 for RE-containing LD formation. Therefore, we made use of another model system, a  
148 *Saccharomyces cerevisiae* mutant strain that lacks the four enzymes responsible for the  
149 last steps in triglyceride - Lro1 and Dga1 - and steryl ester (SE) - Are1 and Are2 -  
150 synthesis. This mutant strain is viable, but does not contain LDs (Sandager et al., 2002).  
151 After introduction of human LRAT into *lro1Δ dga1Δ are1Δ are2Δ* cells (hereafter 4Δ  
152 cells), LRAT-GFP co-localizes with Sec63-mCherry, an ER marker in yeast (Suppl. Fig.  
153 3A). The resulting LRAT expressing yeast cells (4Δ LRAT) were able to synthesize REs  
154 after the addition of ROH (Fig. 2B). In contrast to mammalian cells, the predominant  
155 RE-species was retinyl palmitoleate, RE(16:1). This is in line with the reported fatty acid  
156 composition of PC in yeast, which is capable of producing only monounsaturated fatty  
157 acids, and contains predominantly PC(32:2) and PC(34:2) (Boumann et al., 2006). In the  
158 absence of either LRAT or ROH, both 4Δ and wild-type (*wt*) yeast cells did not  
159 synthesize REs. These results also demonstrate the absence of an endogenous RE  
160 synthase activity in yeast by acyl-CoA retinol acyltransferase (ARAT) activity e.g. Dga1  
161 (Fig. 2B). Thus, RE synthesis in yeast depends on LRAT expression. As anticipated, 4Δ  
162 LRAT yeast cells were devoid of LD structures in the absence of exogenous ROH, as  
163 evidenced by membrane localization of LD-marker Erg6 (Fig. 2C) and BODIPY (Suppl.  
164 Fig. 3B). Upon addition of ROH to 4Δ LRAT yeast cells, we observed a clear presence of  
165 autofluorescent LD-like structures and co-localization of these structures with the  
166 LD-marker Erg6 (Fig. 2C, Suppl. Fig. 3C) and with BODIPY (Suppl. Fig. 3B). In the  
167 absence of LRAT, 4Δ yeast cells could not generate LDs in the presence of ROH.

168 Electron microscopic examination of the LDs generated in  $4\Delta$  LRAT yeast cells revealed  
169 the presence of *bona fide* LDs with a cytosolic orientation that were morphologically  
170 indistinguishable from TAG/SE-filled LDs generated in wt yeast cells (Fig. 2D,E). These  
171 results demonstrate that LRAT induces the formation of LDs in the absence of other LDs  
172 or TAGs (Suppl. Fig. 4). To determine whether retinyl esters can partition into existing  
173 LDs or exclusively form their own LDs, we determined the co-localization of RE positive  
174 LDs (UV<sup>+</sup>) with all LDs (Erg6<sup>+</sup>) immediately after addition of ROH to wt yeast cells  
175 expressing LRAT. These cells have TAG-filled LDs present before addition of ROH. As  
176 shown in Fig. 2F, 2 min after addition of ROH, co-localization of Erg6<sup>+</sup> LDs with UV<sup>+</sup>  
177 LDs was observed. In addition, UV<sup>-</sup> LDs become UV<sup>+</sup> in the next 6 min, indicating that  
178 REs are also transferred into existing LDs.

179

### 180 **Spontaneous nucleation and lens formation of retinyl esters in lipid bilayers**

181 The mechanism of LD formation by LRAT-mediated RE synthesis is not known. For  
182 TAG-filled LDs it has been shown that TAGs have a limited solubility in biological  
183 membranes. Above a critical demixing concentration (~3%), TAG molecules segregate to  
184 form TAG lenses that appear as a first step in LD formation (Choudhary et al. 2015;  
185 Khandelia et al., 2010; Thiam and Forêt, 2016). After this ‘nucleation’ process, the lenses  
186 grow and can emerge from ER membranes during a ‘budding’ process. The formation of  
187 lenses in TAG containing membranes has been demonstrated and studied in molecular  
188 dynamics (MD) simulations (Ben M’barek et al., 2017; Khandelia et al., 2010). Here we  
189 built upon that approach and used coarse-grain MD (CG-MD) simulations of  
190 1-palmitoyl-2-oleoyl-sn-glycero-3-phosphocholine (POPC) membranes with different  
191 amounts of trioleoylglycerol (TOG) and retinyl palmitate (RP) to assess the propensity of  
192 lens formation in those systems. In setups containing only TOG, lens-formation was  
193 consistently observed and always completed within 100 ns of simulation. In contrast,  
194 setups with only RP took considerable longer to nucleate (Fig. 3A) and more often failed  
195 to form lenses on the time scale used for the simulations (250 ns). Lenses formed by RP  
196 were also typically less well defined, with more RP remaining dispersed throughout the  
197 membrane. Mixtures of TOG and RP showed an intermediate efficiency of lens-formation  
198 (Fig. 3A and B). These simulations imply that RP has a lower propensity to self-aggregate,  
199 and hence has a higher nucleation barrier as compared to TOG.

200 Methods to directly measure the nucleation barrier (or ‘critical nucleation volume’) do  
201 not exist, but in a setting with the same PL-composition, the monolayer surface tension  
202 will be a driving force that affects nucleation (Ben M’barek et al., 2017; Deslandes et al.  
203 2017; Thiam and Forêt, 2016). The deformation and budding of a LD monolayer is  
204 controlled in part by the monolayer bending rigidity and surface tension – the monolayer  
205 bending rigidity will tend to flatten a lens, thereby re-dispersing neutral lipid molecules in  
206 the bilayer, while its surface tension will tend to make a lens spherical. However, at a  
207 characteristic size, surface tension will essentially control the monolayer deformation.  
208 This size will be larger for a lower monolayer surface tension: lower monolayer tensions  
209 will likely result in larger ‘critical nucleation volumes’ or higher nucleation barriers (Ben  
210 M’barek et al., 2017; Chorlay and Thiam, 2018; Deslandes et al., 2017; Thiam and Forêt,  
211 2016). We measured the tension of artificial LD containing either RP or TOG and, in line  
212 with our MD simulations, tensions were considerably lower in droplets made of RP as  
213 compared to their TOG counterparts (Table 1). Moreover, droplets surrounded by DOPC

214 with maximum phospholipid packing showed the same trend. These measurements  
215 suggest that RP droplets have higher nucleation barriers, in agreement with the results  
216 obtained by CG-MD.

217 The efficiency of the subsequent budding process of RE-containing LDs can be studied  
218 by determination of budding angles in droplet-embedded vesicles or droplet interface  
219 bilayers (DIBs) containing neutral lipids (Ben M'barek et al., 2017; Chorlay and Thiam,  
220 2018). By using the DIB system, we compared the budding angles of RP-containing lipid  
221 phase with reported values of TAG-LDs (Fig. 3C,D). The budding angles of RP<sup>+</sup> droplets  
222 with PC and PE monolayers did not differ from reported values of their TOG<sup>+</sup>  
223 counterparts (Fig. 3D); angles in the case of PA were only slightly higher. These data  
224 suggest that RP forms spontaneously LDs as efficiently as TG. In PC tensionless  
225 membranes, smaller RP-LD diameters would be thus expected, based on the budding  
226 angles, but the delay in nucleation might introduce an increase in the droplet size. This is,  
227 however, not observed in yeast cells (Fig. 2C). Thus, other factors must contribute to the  
228 characteristic large size of retinyl ester-containing LDs.

229

### 230 **N-terminal sequence of LRAT affects lipid droplet morphology**

231 To study a role of LRAT in LD morphology, we considered the possibility that the  
232 N-terminus of LRAT aids in the formation of LDs. The N-terminal domain of LRAT  
233 (hereafter, LRAT-Nt AH) does not form a trans-membrane domain, despite its high  
234 hydrophobicity (Moise et al., 2007). In addition, it was reported that this domain can  
235 localize to LDs (Jiang and Napoli, 2012). We stably transfected CHO-k1 cells with a GFP  
236 fusion construct of LRAT lacking the N-terminus ( $\Delta$ Nt-LRAT-GFP) and selected clones  
237 with similar GFP fluorescence as compared to CHO-k1 cells stably transfected with  
238 full-length LRAT-GFP (Fig. 1). LRAT-activity of both homogenates was analyzed *in vitro*  
239 using HPLC-MS/MS by determination of RE(7:0) synthesis upon addition of exogenous  
240 PC(7:0/7:0) (Fig. 4A, see Materials and Methods for details). As expected, both enzymes  
241 displayed LRAT-activity with similar  $K_m$ -values for ROH, but reaction rates of  
242  $\Delta$ Nt-LRAT-GFP homogenates were somewhat lower (Fig. 4B). After overnight  
243 incubation with ROH, we observed UV<sup>+</sup> LDs in both cell lines, but LDs appeared smaller  
244 in size in  $\Delta$ Nt-LRAT-GFP expressing cells (Fig. 4C,D). These data show that the  
245 N-terminus is not required *per se* for LD generation, but may have an effect on LD  
246 morphology. To rule out the possibility that the reduced LD size in the presence of  
247  $\Delta$ Nt-LRAT-GFP is caused by the reduced activity of this LRAT mutant (Fig. 4B), we  
248 developed a single-cell imaging analysis pipeline. To this end, we determined cell size,  
249 LD-number per cell and mean LD size per cell by image analysis (see Materials &  
250 Methods for details). Total LD volume (representative for total neutral lipid content) was  
251 calculated from these parameters. Using this approach, we were able to select (“gate”)  
252 cells with similar total LD volume and thus neutral lipid content per cell (Fig. 4E). We  
253 then compared the log-ratios of LD number vs. LD volume per cell of both cell lines  
254 incubated with OA or ROH (Fig. 4F). As expected, no difference was observed when  
255 both cell lines were incubated with OA (Fig. 4F, left panel). In contrast, LDs generated in  
256 the presence of ROH were smaller in size and larger in number in cells expressing  
257  $\Delta$ Nt-LRAT-GFP as compared to LDs from cells expressing the full-length protein, as  
258 reflected by decreased log-ratios (Fig. 4F, right panel). This difference in LD size:number  
259 distribution could also be observed in ungated cells; expressing LD-number as function of



260 the total LD volume per cell showed that regression of all datapoints of LRAT lacking its  
261 N-terminus results in a steeper slope as compared to full-length LRAT, indicating more  
262 LDs per amount of total neutral lipid (Fig. 4G). Taken together, these results show that  
263 the LRAT-Nt has the ability to affect the size: number distribution of retinyl  
264 ester-containing LDs in mammalian cells.

265

### 266 **N-terminus of LRAT exhibits affinity for retinyl esters *in silico***

267 The N-terminus of LRAT is predicted to have an alpha-helical structure without hairpin  
268 topology, which is flanked by amino acids without a clear secondary structure (Suppl. Fig.  
269 5). HeliQuest analysis (Gautier et al., 2008) showed a clear separation between  
270 hydrophobic and polar residues on both sides of the helix, in line with an amphipathic  
271 topology (Fig. 5A, upper panel). However, in comparison with canonical amphipathic  
272 helices involved in membrane recognition (ALPS motifs) (Bigay et al., 2005), the  
273 fraction of hydrophobic over polar residues was considerably higher in the LRAT  
274 N-terminal alpha-helix. This is exemplified by comparison of this projection with CCT- $\alpha$   
275 P2, a recently characterized amphipathic domain with LD-affinity (Prévost et al., 2018)  
276 that contains an ALPS-like architecture (Fig. 5A, bottom panel). The helical wheel  
277 projection of the CCT- $\alpha$  P2 AH revealed a smaller fraction of hydrophobic residues as  
278 compared to the LRAT-Nt AH. Membrane-binding of CCT- $\alpha$  P2 is proportional to the  
279 amount of lipid packing defects (Prévost et al., 2018). We compared the  
280 membrane-binding characteristics of LRAT-Nt with CCT- $\alpha$  P2 by CG-MD using the  
281 DAFT-approach (ensemble of 30 simulations per combination of peptide and model  
282 membrane) (Wassenaar et al., 2015a). One model membrane consisted of POPC and the  
283 other one contained POPC and dioleoylglycerol (DOG), a lipid that induces packing  
284 defects (Vamparys et al., 2013). We subsequently compared membrane binding of both  
285 LRAT-Nt and CCT- $\alpha$  P2. The binding half-time of CCT- $\alpha$  P2 to POPC membranes was  
286 150 ns (Fig. 5B, bottom panel) and in the presence of DOG, this binding was accelerated  
287 (50 nsec) (Fig. 5B, bottom panel), confirming the role of packing defects in membrane  
288 binding (Prévost et al., 2018). For LRAT-Nt, however, we did not observe a difference in  
289 the kinetics of membrane binding between the two model systems (Fig. 5B, top panel;  
290 median of about 60 nsec). Interestingly, the results also showed that LRAT-Nt AH docked  
291 deeper into the bilayer than the CCT- $\alpha$  P2 AH (Fig. 5C), suggesting that LRAT-Nt has the  
292 potential to directly interact with neutral lipids, whereas CCT- $\alpha$  P2 AH binds only to  
293 phospholipids.

294

295 To investigate a potential interaction of the N-terminal peptide with neutral lipids, we  
296 extended the MD setup to a series of POPC membranes containing 10% neutral lipids in  
297 different ratios RP:TOG, and in the presence of LRAT-Nt. The simulations showed that  
298 LRAT-Nt typically co-localized with neutral lipids (Fig. 6A). Inspection of the  
299 localization of LRAT-Nt with respect to the membrane profile (Fig. 6B; Suppl. Fig. 6A)  
300 confirmed that the peptide is docked deep into the membrane. Surprisingly, LRAT-Nt is  
301 docked deeper into the membrane when the neutral lipids consist predominantly of RP as  
302 opposed to TOG (Fig. 6B). This is only partly explained by the thicker membrane  
303 resulting from the more complete lens formation at higher TOG ratios.

304 Initial inspection of the localization of TOGs and RPs within the lens revealed an  
305 asymmetric distribution of the neutral lipid mixture with RPs in closer proximity to the

306 LRAT-Nt peptide (Suppl. Fig. 6B). Assessment of the interaction energies between the  
307 LRAT-Nt helix and both RP and TOG confirmed that the helix has stronger interactions  
308 with RP than it has with TOG (Fig. 6C). This specific affinity of LRAT-Nt for REs could  
309 affect lens and/or LD formation by REs, for example by facilitating the formation of RP  
310 containing lenses by decreasing the nucleation energy barrier. This should then be  
311 reflected in an enhanced nucleation rate. To study such an influence on lens formation,  
312 we performed several series of MD simulations. However, under none of these conditions  
313 LRAT-Nt significantly enhanced the rate of lens formation (data not shown).  
314

### 315 **N-terminus of LRAT exhibits affinity for retinyl esters *in vitro***

316 To study the affinity of the LRAT N-terminus to RP *in vitro*, we synthesized the LRAT-Nt  
317 peptide and assessed its recruitment to RP vs. TOG interface. Oil-in-water droplets were  
318 formed and the peptide was added (Fig. 7A). Recruitment of the peptide to the droplet  
319 interface will decrease the interfacial surface tension (Fig. 7A) (Ajjaji et al., 2019; Small,  
320 Wang, & Mitsche, 2009), which happened for both RP and TOG (Fig. 7B). Tension  
321 reached an equilibrium value which corresponds to the maximum of adsorbed peptides  
322 (9.2 mN/m for TOG, and 6.1 mN/m for RP). The peptide recruitment level is determined  
323 by the neutral lipid affinity for LRAT-Nt. To further investigate this, we performed a rapid  
324 compression experiment whereby, at the equilibrium interfacial tension, the droplet  
325 interface was reduced by decreasing its volume (Fig. 7C,D, left, dotted lines). This  
326 operation transiently increased the interfacial lateral pressure, *i.e.* the peptide surface  
327 density, and we recorded the relaxation of the system to equilibrium. During compression,  
328 surface tension decreased in the case of TOG, reached a transient plateau and  
329 subsequently continued decreasing (Fig. 7C). Appearance of the plateau is a signature of  
330 a rearrangement of the peptide at the surface, induced by the increase of its surface  
331 density (Mitsche & Small, 2013). As soon as compression was stopped, surface tension  
332 increased again, which is a signature of the desorption of some of the peptides from the  
333 surface. This behavior at the TOG interface is unique to LRAT-Nt, as the 11mer repeat  
334 domain of Plin1 does not show such response under similar experimental procedures  
335 (Ajjaji et al., 2019). With RP, compression led to a continuous decrease of tension (Fig.  
336 7D) and upon arrest of compression, tension remained constant: the peptide did not  
337 desorb from the interface. These results confirm the MD simulations and show that the  
338 LRAT-Nt peptide interacts with neutral lipids and with a preference for retinyl esters.

339

## 340 Discussion

341 Lipid droplet formation starts when neutral lipids accumulate within the bilayer of  
342 biological membranes above the a critical demixing concentration (Thiam and Forêt,  
343 2016; Walther et al., 2017). Although the intrinsic capacity of different classes of neutral  
344 lipids to form LDs is well accepted based on biophysical considerations (Ben M'barek et  
345 al., 2017), *in vivo* this has only been demonstrated for triacylglycerols in yeast (Sandager  
346 et al., 2002). As cholesteryl ester synthesizing enzymes also contribute to TAG synthesis,  
347 it remains to be established whether cholesteryl esters are capable of forming lipid  
348 droplets in the absence of triacylglycerols (Sandager et al., 2002). Here we show the  
349 existence of an alternative route for LD biogenesis, in which synthesis of another class of  
350 neutral lipids, retinyl esters, is sufficient to drive LD formation.

351 Based on biophysical properties of retinyl esters, we show that the spontaneous  
352 nucleation of retinyl ester-generated LDs is somewhat less efficient as compared to TAGs.  
353 Indeed, molecular dynamic simulations (Fig. 3 A,B) and *in vitro* experiments measuring  
354 the tension of artificial droplet interfaces (Table 1) suggest that RP droplets have a higher  
355 nucleation barrier, or lower nucleation efficiency than TAGs. Despite these biophysical  
356 considerations, retinyl ester-filled LDs are efficiently formed upon exogeneous induction  
357 of LRAT in yeast cells that lack the machinery to synthesize TAG/SE-filled LDs (Fig. 2).  
358 Surprisingly, the LRAT protein itself is involved in the generation of the large sized LDs  
359 that are characteristic for retinyl ester-containing LDs.

360  
361 LRAT is broadly expressed with highest expression levels in the intestine, liver, testis and  
362 eye (Liu and Gudas, 2005; Ruiz et al., 1999). The majority of dietary vitamin A (~75%) is,  
363 however, taken up by hepatocytes (Gottesman et al., 2001) and stored as retinyl esters in  
364 the liver, primarily in hepatic stellate cells (Blaner et al., 2009; Blomhoff et al., 1991;  
365 Friedman, 2008; Gottesman et al., 2001; Ross and Zolfaghari, 2004). LRAT expression is  
366 the highest in quiescent HSCs (Fig. 1E), in agreement with previous reports (Mederacke  
367 et al., 2013), but this expression is rapidly lost upon activation of HSCs. LRAT  
368 expression thus coincides with the presence of large LDs in quiescent HSCs. When LRAT  
369 expression is reduced (in activated HSCs, Fig. 1E) or absent in LRAT<sup>-/-</sup> mice (Ajat et al.,  
370 2017; O'Byrne et al., 2005), HSCs lack their characteristic large LDs. These findings  
371 show that the presence of LRAT correlates with the existence of the large LDs, consistent  
372 with the data now presented here.

373  
374 LRAT belongs to the papain-like or NlpC/P60 thiol protease superfamily of proteins  
375 (Anantharaman and Aravind, 2003). The H-RAS-like suppressor (HRASLS) enzymes,  
376 also known as LRAT-like proteins comprise a vertebrate subfamily that includes LRAT  
377 and that function in acyl chain remodeling of phospholipids (Golczak et al., 2012;  
378 Mardian et al., 2015). The *in vivo* biological substrates and activities of most family  
379 members have not yet been elucidated. LRAT is the best characterized family member,  
380 which catalyzes the formation of retinyl esters by transferring an acyl group from the *sn-1*  
381 position of PC onto ROH. The substrate specificity of LRAT for PC as acyl donor is  
382 intriguing. LD size is regulated by several factors including PC synthesis (Krahmer et al.,  
383 2011). During LD growth, the expanding LD monolayer activates CTP:Phosphocholine  
384 cytidyltransferase, a key enzyme in PC synthesis. LRAT degrades PC which may result  
385 in activation of the same PC synthesizing pathway. Alternatively, reduced PC

386 concentrations may either destabilize LDs and induce coalescence of LDs or increase ER  
387 bilayer tension, thereby generating larger (merged) LDs. Concomitant with retinyl ester  
388 production, however, PC is converted to lyso-PC. The bilayer surface tension is reduced  
389 by lyso-phospholipids, facilitating LD budding and reducing LD size (Ben M'barek et al.,  
390 2017). Thus, counteracting forces contributing to LD size are involved in the generation  
391 of retinyl ester-loaded LDs. The N-terminus of LRAT tips the balance as it is required for  
392 the generation of large LDs in mammalian cells. The effect of the N-terminus of LRAT on  
393 LD size is specific for retinyl ester-mediated LD formation: despite its presence in  
394 CHO-k1 LRAT-GFP cells, it does not affect the size of TAG filled LDs (Fig. 4).  
395 Since the N-terminus of LRAT does not seem to affect the rate of LD formation, it could  
396 change the thermodynamic equilibrium and decreases the nucleation concentration. As a  
397 result, it would then also dictate where LD formation occurs. However, we did not  
398 observe a colocalization of LRAT with nascent LDs (data not shown). Therefore, we  
399 consider it more likely that the observed specific affinity of the LRAT N-terminus for  
400 retinyl esters is likely to play an important role in affecting LD size, for example by  
401 changing the membrane topology of LRAT. LRAT is anchored to the ER membrane by a  
402 single transmembrane spanning domain at the C-terminus and with the catalytic domain  
403 and the N-terminus oriented towards the cytoplasm (Moise et al., 2007). The production  
404 of retinyl esters results in a strongly enhanced membrane binding of the N-terminus as  
405 illustrated by the deeper embedding of the N-terminus in the membrane, combined with  
406 the specific interaction with retinyl esters. Indeed, in the absence of the N-terminus,  
407 LRAT maintains retinyl ester production but fails to generate large LDs. In addition to a  
408 direct interaction with retinyl esters, it can however not be excluded that the N-terminus  
409 of LRAT also affects lipid droplet size by interfering with other mechanisms such as  
410 lipolysis and/or lipogenesis.

411 In summary, the molecular design of LRAT is well suited to store retinyl esters in LDs.  
412 With its C-terminal transmembrane domain, LRAT is anchored in the endoplasmic  
413 reticulum and directs newly synthesized retinyl esters in the lipid bilayer. The retinyl  
414 esters have the intrinsic capacity to form lipid droplets and with the N-terminal  
415 hydrophobic peptide LRAT specifically affects the size of retinyl ester-loaded lipid  
416 droplets.

417  
418  
419

420 **Acknowledgments**

421 We thank Shreyas Sinha and Elmon Meijering for their assistance during the initial phase  
422 of experiments. Microscopy images were acquired at the Center of Cellular Imaging,  
423 Faculty of Veterinary Medicine, Utrecht University, we thank Esther van 't Veld for the  
424 technical assistance. Lipid analyses were performed at the Lipidomics Centre, Faculty of  
425 Veterinary Medicine, Utrecht University, we thank Jeroen Jansen for the technical  
426 assistance.

427

428 **Author Contributions**

429 Conceptualization: J.B.H.; Methodology: M.R.M., T.A.W., A.R.T., W.A.P., J.B.H.;  
430 Software: T.A.W.; Formal Analysis: M.R.M., T.A.W.; Investigation: M.R.M., T.A.W.,  
431 K.K.Y., A.T., M.C.M., L.C., A.C., M.W.H.; Writing – Original Draft: M.R.M., J.B.H.;  
432 Writing – Review & Editing: M.R.M., M.H., A.B.V., A.R.T., W.A.P., J.B.H.;  
433 Visualization: M.R.M., T.A.W., K.K.Y., M.C.M., L.C., A.C., R.W.W.; Supervision:  
434 M.H., A.B.V., F.R., A.R.T., W.A.P., J.B.H.; Project Administration: J.B.H.

435

436 **Declaration of Interests**

437 The authors declare no competing interests.

438

439

## 440 **Material & Methods**

441

### 442 **Hepatic stellate cells isolation and cell culturing**

443 Hepatic stellate cells (HSCs) were isolated from 10–12 week-old male mice (C57BL/6J  
444 background, wild-type pups from crossed LRAT<sup>+/-</sup> heterozygote (Liu and Gudas, 2005  
445 mice) as described before (Riccaltón-Banks et al., 2003). Animals were handled  
446 according to governmental and international animal experimentation guidelines and laws.  
447 Experiments were approved by the Animal Experimentation Committee  
448 (Dierexperimentencommissie; DEC) of Utrecht University (DEC number  
449 2013.III.02.016). After isolation, cells were protected from light and cultured on  
450 coverslips in 24-wells plates (Nunc, Roskilde, Denmark) in Dulbecco Modified Eagle  
451 Medium (DMEM) supplemented with 10% fetal bovine serum (FBS), 100 U/mL  
452 penicillin and 100 µg/mL streptomycin (all obtained from Gibco, Invitrogen GmbH,  
453 Lofer, Germany).

454 CHO-k1 cells were cultured in Ham's F-12 medium supplemented with 7.5% FBS, 100  
455 units/ml penicillin, and 100 µg/mL streptomycin. The human hepatic stellate cell line  
456 LX-2 cells (kindly donated by Dr. Friedman (New York, NY, USA)) were grown in  
457 DMEM containing 10% FBS, 100 U/mL penicillin and 100 µg/mL streptomycin. All cells  
458 were maintained in a humidified incubator (5% CO<sub>2</sub>) at 37 °C. Depending on the  
459 experiment, cells were incubated with retinol (Sigma, stocks of 30 mM in EtOH), oleic  
460 acid (Sigma) coupled to fatty acid free-BSA (Sigma, stocks of 10 mM fatty acid in 12%  
461 BSA) and/or triacsin C (Cayman, stocks of 1 mg/mL in DMSO).

462

### 463 **Retinol handling**

464 Retinol (Sigma) was dissolved in ethanol (30 mM) and stored in 50 µL aliquots at -80°C.  
465 We routinely measured UV absorption spectra of retinol stocks before use and calculated  
466 the current stock concentration by making use of the molar extinction coefficient of  
467 retinol in EtOH (52,480 mol L<sup>-1</sup> cm<sup>-1</sup> at 325 nm) (Ross AC, 1981). In addition, we made  
468 use of the observation that after exposure to UV-light, a peak around 240 nm emerged,  
469 accompanied with a decrease around 325 nm. We routinely monitored E<sub>325</sub>/E<sub>240</sub> ratios and  
470 used exclusively stocks with a ratio of 5 or higher, which was estimated to correspond  
471 with a retinol integrity of about 70%.

472

### 473 **Generation of stable cell lines**

474 Human LRAT cDNA was synthesized and cloned into a pcDNA3.1(+) vector (Clontech,  
475 Palo Alto, California, USA) by a third party (GeneArt, Thermo Fisher Scientific,  
476 Waltham, MA, USA). In addition, the LRAT sequence was cloned into a pEGFP-N2  
477 vector (Clontech), resulting in LRAT fused to the N-terminus of GFP. The construct  
478 coding for the deletion mutant ( $\Delta$ Nt-LRAT-GFP) was generated by site directed  
479 mutagenesis (New England Biolabs, Ipswich, MA). CHO-k1 and LX-2 cells were  
480 transiently transfected by Lipofectamine 2000 (Thermo Fisher) according to the  
481 manufacturer's instructions. Stable CHO-k1 cells expressing the various LRAT variants  
482 or control GFP were generated as follows. Cells (2x10<sup>6</sup>) were electroporated in PBS with  
483 15 µg DNA and a pulse of 260 V. After plating, cells were cultured for 48h in the absence  
484 and for 3 weeks in the presence of 1 mg/mL G-418 selection antibiotic (Thermo Fisher).  
485 Stable cells expressing GFP-fusion proteins were trypsinized and single GFP<sup>+</sup> cells with

486 scatter properties (FSC and SSC) similar to their non-transfected counterparts were plated  
487 into 96-wells plates by FACS (Influx Cell Sorter, BD Biosciences). A GFP-negative gate  
488 was chosen to select monoclonal stable cells expressing non-fluorescent proteins. After  
489 plating, the monoclonal cells were allowed to grow until wells reached confluency.  
490 Clones with comparable morphology as compared to parental CHO-k1 cells (cell size,  
491 nucleus, lipid droplets) were selected. The absence or presence of LRAT enzymatic  
492 activity in LRAT, GFP, LRAT-GFP and  $\Delta$ Nt-LRAT-GFP expressing clones was confirmed  
493 by determination of retinyl esters (see below) and UV<sup>+</sup>-autofluorescent lipid droplets in  
494 combination with GFP-fluorescence by FACS (FACSCanto II, BD Biosciences) after  
495 incubation of cells with retinol.

496

### 497 **Confocal microscopy of mammalian cells**

498 Cells were plated on Lab-Tek II 8-chamber slides (Thermo Fisher) and incubated as  
499 described in the figure legends. Cells were fixed in 4% paraformaldehyde (Electron  
500 Microscopy Sciences Hatfield, PA, USA). Subsequently, cells were stained with either  
501 DAPI, BODIPY 493/503 (Thermo Fisher), and/or LD540 (kindly donated by Dr. C.  
502 Thiele, Bonn, Germany) (Spandl et al., 2009). Staining for immunofluorescence was  
503 performed with anti-desmin or anti- $\alpha$  smooth muscle actin (both from Thermo Scientific),  
504 followed by goat-anti-mouse-alexa647 or donkey-a-rabbit-alexa647 (Life Technologies,  
505 Paisley, UK). Cells were mounted with FluorSave (Calbiochem, Billerica, MA, USA) and  
506 subsequently imaged with a Leica TCS SPE Laser Scanning Spectral Confocal  
507 Microscope (Wetzlar, Germany) or a Nikon A1R confocal microscope (Amsterdam, The  
508 Netherlands) using preset settings for the representative dyes. For the detection of  
509 retinoid autofluorescence, presets for DAPI were used.

510

### 511 **Quantification of cells with lipid droplet parameters**

512 To quantify cells and lipid droplets, z-series of cells were imaged in tile-scan mode.  
513 Datasets were generated with either CellProfiler v2.2.0 (Kamentsky et al., 2011) or Imaris  
514 v8.2.0 (Bitplane, Belfast, Northern Ireland), both resulting in the identification of lipid  
515 droplets associated with individual cells. Data were subsequently expressed for individual  
516 cells containing ‘cell size’ (diameters of cells, in arbitrary units), ‘number of lipid droplets  
517 per cell’, ‘mean lipid droplet volume per cell’ (mean of all LD diameters of the cell to the  
518 3<sup>rd</sup> power, in arbitrary units) and ‘total lipid droplet volume per cell’ (product of ‘number  
519 of lipid droplets per cell’ and ‘mean lipid droplet volume per cell’, in arbitrary units).  
520 Subsequently, the resulting data were processed with R v3.4.4 and RStudio v1.0.153  
521 using R-packages ‘openCyto’ v1.14.0, ‘reshape2’ v1.4.2 and ‘ggplot2’ v2.2.1.  
522 To analyze the lipid droplet size distribution, lipid droplet diameters were not linked to  
523 individual cells, but analyzed per condition. Ranges of LD-diameter bins were calculated  
524 using the limits of the first, second, third, fourth and fifth diameter quintile of all lipid  
525 droplets. LD-presence in each bin was counted per condition and expressed as percentage  
526 (all lipid droplets per condition were set to 100%).

527

### 528 **Structured illumination microscopy (3D-SIM)**

529 After treatment, cells were stained with DAPI and HCS LipidTOX Red Neutral Lipid  
530 Stain (Thermo Fisher) and mounted with Vectashield Antifade Mounting Medium (Vector  
531 Laboratories, Burlingame, CA, USA). Structured illumination microscopy was performed

532 using a Deltavision OMX-V4 Blaze (GE Healthcare, Chicago, IL, United States) setup  
533 equipped with 4 sCMOS (PCO) cameras. Immersion oil with 1.516 refractive index (GE  
534 Healthcare) was placed on the 60x objective (Olympus U-PLAN APO, NA 1.42).  
535 Fluorophores were excited with a diode 405 nm (Vortran Stradus, 100 mW) and an OPSL  
536 568 nm (Coherent, 100 mW) laser modulated to 1% by Neutral density filters. System  
537 supplied filter blocks were used to acquire fluorescence of DAPI (Ex: 382-409, Em:  
538 421-450) and LipidTOX Red (Ex: 561-580, Em: 591-627). Raw images were processed  
539 using SoftWoRx software (GE Healthcare) with system OTFs pre-determined with 100  
540 nm fluorescent polystyrene beads (Thermo scientific) and camera alignment parameters  
541 for the different channels (see supplemental materials). Acquired images were  
542 deconvolved using default settings (omitting Wiener filtering and background subtraction)  
543 including negative values (supplied as such in supplemental data) and intensities were  
544 linearly adjusted. Images in the figures are supplied as maximum intensity projections  
545 (movies are in supplemental data).

546

#### 547 **Lecithin:retinol acyltransferase activity assay**

548 Lecithin:retinol acyltransferase activity in homogenates expressing various LRAT  
549 variants was performed as described previously (Golczak et al., 2015). Briefly, cells were  
550 cultured overnight in T-75 culture flasks (CELLSTAR, Greiner Bio-One GmbH,  
551 Frick-enhausen, Germany) under normal cell growth conditions. After scraping in  
552 ice-cold PBS, cells were homogenized on ice with 26-gauge needles (BD Bioscience, San  
553 Jose, CA, USA). Homogenates containing 200 µg total protein were mixed with reaction  
554 mix containing 5 mM DTT, 5 mM EDTA, 10 mM Tris-HCl (pH 8.0), 1% BSA, 0.2 µM  
555 ascorbic acid, 2 mM PC(7:0/7:0) and increasing amounts of retinol. Subsequently,  
556 mixtures were incubated for 60 min at 37°C in amber glass vials. Levels of retinyl  
557 heptanoate were determined by LC-MS/MS (see below).  $K_m$  and  $v_{max}$  values were  
558 estimated using Michaelis-Menten kinetics.

559

#### 560 **Retinoids and neutral lipid determination by LC-MS/MS**

561 Lipids were extracted as previously described (Bligh and Dyer, 1959). To avoid  
562 photo isomerization and oxidation of the retinoids, extractions were performed under red  
563 light and in amber tubes. In addition, 1 nmol butylated-hydroxytoluene was added to  
564 every sample. As internal standard, 250 pmol of retinyl acetate in MeOH/CHCl<sub>3</sub> (1:1, v/v)  
565 was added. The combined chloroform phases were dried under nitrogen and stored at  
566 - 20 °C until further analysis.

567 Extract were dissolved in MeOH/CHCl<sub>3</sub> (1:1) and stored in amber autosampler vials. To  
568 measure retinoids, samples were injected and separated on a 250 × 3.0 mm Synergi™ 4u  
569 Max-RP 80A column (4 µm particle size, Phenomenex, CO, USA) with a flow rate of  
570 350 µL min<sup>-1</sup>. To this end, a gradient (solvent A; acetonitrile:water (95:5), solvent B;  
571 acetone:chloroform (85:15), 0 min; 90% A, 5 min; 40% A, 17 min; 0% A, 19 min; 90% A,  
572 25 min; 90% A) was generated by a Flexar UHPLC system (Perkin Elmer, Waltham, MA,  
573 USA). The column outlet was connected to a triple quadrupole mass spectrometry (API  
574 4000 QTRAP, MDS Sciex/Applied Biosystems, Foster City, Canada) with an atmospheric  
575 pressure chemical ionization (APCI) ionization source (set to 500 °C). Multiple reaction  
576 monitoring (MRM) in positive ion mode was used to detect retinyl ester species with  
577 settings and m/z transitions as described before (Ajat et al., 2017). Chromatographic



578 peaks were integrated and quantified using Analyst software version 1.4.3 (Applied  
579 Biosystems, Foster City, Canada).  
580 To measure other neutral lipids (sterols, triacylglycerols, steryl esters), samples were  
581 injected and separated on a Kinetex/HALO C8 column (2.6  $\mu\text{m}$ , 150  $\times$  3.00 mm;  
582 Phenomenex, Torrance, CA, USA). A gradient of methanol:H<sub>2</sub>O (5:5 v/v, solvent A) and  
583 methanol:isopropanol (8:2 v/v, solvent B) was generated by an Infinity II 1290 UPLC  
584 (Agilent, Santa Clara, CA, USA) and with a constant flow rate of 600  $\mu\text{L min}^{-1}$  (0 min;  
585 100% A, 2 min; 0% A, 8 min; 0% A, 8.5 min; 100% A, 10 min; 100% A). Lipids were  
586 measured using APCI in positive mode coupled to an Orbitrap Fusion mass spectrometer  
587 (Thermo Scientific, Waltham, MA, USA). Vendor data files were converted to  
588 mzML-format with msConvert (part of ProteoWizard v3.0.913) and processed with  
589 XCMS Online v3.7.0 (Tautenhahn et al., 2012).  
590

### 591 **Growth and fluorescence microscopy of yeast**

592 Yeast strains and plasmids used in this study are described in Supplemental Table 1. Yeast  
593 were grown at 30°C in synthetic complete media containing 0.67% yeast nitrogen base  
594 without amino acids (United States Biological), 2% glucose, and an amino acid mix  
595 (United States Biological). Retinol (Sigma-Aldrich) was added to the medium at 4 mM  
596 together with 1% Igepal CA-630 (Sigma-Aldrich). Cells were stained with 0.5  $\mu\text{g/ml}$   
597 BODIPY 493/503 (Invitrogen) for 10 min and being washed once with phosphate  
598 buffered saline.

599 Yeast were imaged at 30 °C in an Environmental Chamber with a DeltaVision Spectris  
600 (Applied Precision Ltd.) comprising a wide-field inverted epifluorescence microscope  
601 (IX70; Olympus), a 100  $\text{\AA}$ ~ NA 1.4 oil immersion objective (UPlanSAPO; Olympus),  
602 and a charge-coupled device Cool-Snap HQ camera (Photometrics).  
603

### 604 **Western blot analysis**

605 Cells expressing LRAT-GFP and  $\Delta\text{N-LRAT-GFP}$  were growth to logarithmic growth  
606 phase and 10 OD600 units of cells were washed once with H<sub>2</sub>O and lysed with glass beads  
607 in a Precellys 24 homogenizer (Bertin Instruments). The lysate was cleared by  
608 centrifugation at 500  $x$  g for 10 minutes at 4°C. The protein concentration of the lysate  
609 was determined using a Bradford assay (Thermo Scientific) and 10  $\mu\text{g}$  of protein were  
610 separated by 4–12% of SDS-PAGE gel (Invitrogen), and transferred to nitrocellulose  
611 membranes at 120 V for 2 h. The membrane was analyzed using primary antibodies to  
612 GFP (1:1,000; Roche) and anti-porin (1:1,000; Invitrogen). Proteins were visualized using  
613 IRDye secondary anti-mouse antibody (Li-COR Biosciences; 1:10,000). The blots were  
614 visualized with an Odyssey infrared imaging system (Li-COR Biosciences).  
615

### 616 **LRAT mRNA expression by quantitative PCR**

617 Expression of LRAT mRNA was determined as described (Tuohetahuntala et al., 2017).  
618 Briefly, RNA was isolated with a RNeasy Micro Kit (Qiagen, Venlo, The Netherlands)  
619 and cDNA was synthesized with an iScript cDNA Synthesis Kit (Bio-Rad). PCR  
620 amplifications were performed using a Bio-Rad detection system with iQ SYBR Green  
621 Supermix (Bio-Rad, Veenendaal, The Netherlands). Gene expression was normalized  
622 against reference genes, sequences of the primers are listed in Suppl. Table 2.

623

624

### 625 **Molecular dynamics**

626 MD simulations were set up and run using the DAFT protocol (Wassenaar et al., 2015a),  
627 according to procedures for building membrane/solvent systems using INSANE  
628 (Wassenaar et al., 2015b) and for generating membrane/solvent/protein systems as  
629 described in (Wassenaar et al., 2015a). The latter comprises a step for the generation of  
630 the LRAT-Nt peptide (sequence  
631 MKNPMLLEVVSLLLEKLLLLISNFTLFSSGAAGEDKGRNSF; secondary structure  
632 LLLHHHHHHHHHHHHHHHHLLLLLLLLLLLLLLLLLLLL) or the CCT $\alpha$  P2 peptide  
633 (sequence VEEKSIDLIQKWEEKSREFIGSFLEMFG; secondary structure  
634 HHHHHHHHHHHHHHHHHHHHHHHHHHHHHHHHH), which was placed horizontally above  
635 the membrane. For docking simulations, the helix was placed at a distance 4 nm from the  
636 bilayer center with random rotation around the helix axes, while for assessment of the  
637 effect on lens formation speed, the helix was placed at 2.5 nm from the bilayer center,  
638 with the hydrophobic side facing towards the membrane. Simulations were performed  
639 using the coarse grain Martini 2.2 model (Marrink et al., 2004, 2007; Monticelli et al.,  
640 2008).

641 Simulations for assessing binding of LRAT-Nt AH to membranes with different  
642 compositions were set up in a hexagonal prism unit cell with a total number of 250 lipids  
643 per leaflet and a height of 9 nm. Simulations for assessing the lens forming propensity  
644 and speed, were set up in a hexagonal prism unit cell with base length of 24 nm and  
645 height of 10 nm, regardless of the presence or absence of protein. Numbers or ratios or  
646 lipids were set as described in the main text. All simulations were performed using  
647 Gromacs 2018.x (Pronk et al., 2013), using the automated Martini workflow *martinate*  
648 (Wassenaar et al., 2013).

649

### 650 **Electron Microscopy**

651 Yeast cells were grown in synthetic drop-out media lacking leucine at 30°C to an OD<sub>600</sub>  
652 of approximately 0.6. IGEPAL (Sigma-Aldrich) was added to the cell cultures to a final  
653 concentration of 1%, prior to addition of retinol (Sigma-Aldrich) to a final concentration  
654 of 2 mM. Cells were then incubated for 10 min at 30°C before being processed for  
655 electron microscopy as follow. Cells were chemically fixed, embedded with 12% gelatin,  
656 cryo-sectioned and stained as previously described (Griffith et al., 2008). Sections were  
657 imaged in a FEI CM100bio electron microscope at 80 KV, equipped with a digital camera  
658 (Morada; Olympus). Two different grids with sections obtained from the same  
659 preparation were statistically evaluated by counting 75 randomly selected cell profiles  
660 before determining the average number of lipid droplets per cell section plus standard  
661 deviation between the two grids.

662

### 663 **Monolayer tension measurements**

664 Tension measurements were performed using a drop tensiometer device (Tracker,  
665 Teclis-IT Concept, France) (Ben M'barek et al., 2017). The principle of the drop profile  
666 analysis is based on the determination of the shape of a liquid drop suspended in another  
667 liquid form from a video image and its comparison with theoretical profiles calculated  
668 from the Gauss Laplace equation. The retinyl palmitate (Sigma, R-1512) drop (neutral

669 lipid phase), with or without containing the DOPC phospholipid, was formed in buffer  
670 (50mM HEPES, 120mM potassium acetate, 1mM magnesium chloride, pH 7.4) at room  
671 temperature. The tension was allowed to stabilize for a few minutes (it decreases by the  
672 continuous absorption of phospholipids to the oil/water interface). Then, the drop is  
673 compressed by decreasing its volume, until complete saturation of the interface is reached  
674 (marked by a plateau of tension during compression).

675

### 676 **Droplet interface bilayer (DIB) experiments**

677 The DIB experiments was performed following the previous study of (Ben M'barek et al.,  
678 2017). An oil phase containing phospholipids was prepared first. DOPC, DOPE and  
679 DOPA were purchased from Avanti Polar Lipids, Inc. Lipids were mixed to the RP  
680 (Sigma, R-1512) oil at a final lipid concentration of 0.2% w/w (about 10% chloroform  
681 was in the final mixture in the case of DOPC initial stabilization of the DIBs, and we let it  
682 evaporate over time; for the other phospholipids, chloroform was evaporated prior to  
683 addition of RP). Then, an emulsion was prepared mixing the buffer with RP (1:5 v/v).  
684 Finally, the same volumes of emulsion and phospholipids in RP were put together, and  
685 the resulting emulsion was placed on a hydrophobic coverslip.

686

### 687 **Interfacial tension measurements**

688 A pendent droplet tensiometer designed by Teclis Instruments (Longessaigne, France)  
689 was used to measure the interfacial tension of oil/water interfaces. All experiments were  
690 conducted at room temperature. To create oil/buffer interfaces, oil drops (10 $\mu$ L) were  
691 formed at the tip of a J-needle submerged in 5 mL of HKM buffer.

692 *Oil-peptide surface tension measurement:* 10  $\mu$ l of LRAT peptide solution in DMSO was  
693 added to the bulk buffer while the tension of trioleoylglycerol/buffer or retinyl  
694 palmitate/buffer interface was measured. The resulting concentration of peptide was 4.6  
695  $\mu$ M for both retinyl palmitate and trioleoylglycerol experiments. Oil-peptide surface  
696 tension was determined when the interfacial tension was stabilized.

697 After tension stabilization, the interface is compressed. The compression was then  
698 stopped, and area was kept constant as interfacial tension was recorded. Relaxation of the  
699 tension was observed only for trioleoylglycerol/buffer interfaces. Human LRAT peptide  
700 (AA 1-39) was synthesized by Bio-Synthesis (Lewisville, Texas, USA).

701

### 702 **Statistical analyses**

703 All figures were built in RStudio v1.0.153 (R v3.4.4) and processed in Inkscape v0.92.2.  
704 Barplots represent means  $\pm$  standard deviation (SD) or standard error of the mean (SEM)  
705 as indicated in the figure legends. Statistical significance was determined by two-tailed  
706 paired or unpaired Welch's t-test or Wilcoxon rank sum test, or by Pearson's Chi-squared  
707 test, as indicated. In experiments with multiple testing, P-values were corrected by the  
708 Benjamini-Hochberg procedure. P-values below 0.05 were considered statistically  
709 significant.

710

711

## 712 **References**

- 713 Ajat, M., Molenaar, M., Brouwers, J.F.H.M., Vaandrager, A.B., Houweling, M., and  
714 Helms, J.B. (2017). Hepatic stellate cells retain the capacity to synthesize retinyl esters  
715 and to store neutral lipids in small lipid droplets in the absence of LRAT. *Biochim.*  
716 *Biophys. Acta 1862*, 176–187.
- 717 Ajjaji, D., Ben M’barek, K., Mimmack, M.L., England, C., Herscovitz, H., Dong, L., Kay,  
718 R.G., Patel, S., Saudek, V., Small, D.M., et al. (2019). Dual binding motifs underpin the  
719 hierarchical association of perilipins1-3 with lipid droplets. *Mol. Biol. Cell 30*, 703–716.
- 720 Anantharaman, V., and Aravind, L. (2003). Evolutionary history, structural features and  
721 biochemical diversity of the NlpC/P60 superfamily of enzymes. *Genome Biol.* 1–12.
- 722 Ben M’barek, K., Ajjaji, D., Chorlay, A., Vanni, S., Forêt, L., and Thiam, A.R. (2017).  
723 ER Membrane Phospholipids and Surface Tension Control Cellular Lipid Droplet  
724 Formation. *Dev. Cell 41*, 591–604.e7.
- 725 Bigay, J., Casella, J.-F., Drin, G., Mesmin, B., and Antonny, B. (2005). ArfGAP1  
726 responds to membrane curvature through the folding of a lipid packing sensor motif.  
727 *EMBO J. 24*, 2244–2253.
- 728 Blaner, W.S., O’Byrne, S.M., Wongsiriroj, N., Kluwe, J., D’Ambrosio, D.M., Jiang, H.,  
729 Schwabe, R.F., Hillman, E.M.C., Piantedosi, R., and Libien, J. (2009). Hepatic stellate  
730 cell lipid droplets: a specialized lipid droplet for retinoid storage. *Biochim. Biophys. Acta*  
731 *1791*, 467–73.
- 732 Bligh, E.G., and Dyer, W.J. (1959). A rapid method of total lipid extraction and  
733 purification. *Can. J. Biochem. Physiol. 37*, 911–917.
- 734 Blomhoff, R., Green, M.H., Green, J.B., Berg, T., and Norum, K.R. (1991). Vitamin A  
735 metabolism: new perspectives on absorption, transport, and storage. *Physiol. Rev. 71*,  
736 951–990.
- 737 Boumann, H.A., Gubbens, J., Koorengel, M.C., Oh, C.-S., Martin, C.E., Heck, A.J.R.,  
738 Patton-Vogt, J., Henry, S.A., de Kruijff, B., and de Kroon, A.I.P.M. (2006). Depletion of  
739 phosphatidylcholine in yeast induces shortening and increased saturation of the lipid acyl  
740 chains: evidence for regulation of intrinsic membrane curvature in a eukaryote. *Mol. Biol.*  
741 *Cell 17*, 1006–17.
- 742 Chelstowska, S., Widjaja-Adhi, M.A.K., Silvaroli, J.A., and Golczak, M. (2017). Impact  
743 of LCA-Associated E14L LRAT Mutation on Protein Stability and Retinoid Homeostasis.  
744 *Biochemistry (Mosc.) 56*, 4489–4499.
- 745 Chorlay, A., and Thiam, A.R. (2018). An Asymmetry in Monolayer Tension Regulates  
746 Lipid Droplet Budding Direction. *Biophys. J. 114*, 631–640.

- 747 Choudhary, V., Ojha, N., Golden, A., and Prinz, W.A. (2015). A conserved family of  
748 proteins facilitates nascent lipid droplet budding from the ER. *J. Cell Biol.* *211*, 261–271.
- 749 Deslandes, F., Thiam, A.R., and Forêt, L. (2017). Lipid Droplets Can Spontaneously Bud  
750 Off from a Symmetric Bilayer. *Biophys. J.* *113*, 15–18.
- 751 Friedman, S.L. (2008). Hepatic Stellate Cells : Protean , Multifunctional , and Enigmatic  
752 Cells of the Liver. *Phys. Rev.* 125–172.
- 753 Gautier, R., Douguet, D., Antonny, B., and Drin, G. (2008). HELIQUEST: a web server  
754 to screen sequences with specific alpha-helical properties. *Bioinforma. Oxf. Engl.* *24*,  
755 2101–2102.
- 756 Golczak, M., Kiser, P.D., Sears, A.E., Lodowski, D.T., Blaner, W.S., and Palczewski, K.  
757 (2012). Structural basis for the acyltransferase activity of lecithin:retinol  
758 acyltransferase-like proteins. *J. Biol. Chem.* *287*, 23790–807.
- 759 Golczak, M., Sears, A.E., Kiser, P.D., and Palczewski, K. (2015). LRAT-specific domain  
760 facilitates vitamin A metabolism by domain swapping in HRASLS3. *Nat. Chem. Biol.* *11*,  
761 26–32.
- 762 Gottesman, M.E., Quadro, L., and Blaner, W.S. (2001). Studies of vitamin A metabolism  
763 in mouse model systems. *BioEssays* *23*, 409–419.
- 764 Griffith, J., Mari, M., Mazière, A.D., and Reggiori, F. (2008). A Cryosectioning  
765 Procedure for the Ultrastructural Analysis and the Immunogold Labelling of Yeast  
766 *Saccharomyces cerevisiae*. *Traffic* *9*, 1060–1072.
- 767 Hashemi, H.F., and Goodman, J.M. (2015). The life cycle of lipid droplets. *Curr. Opin.*  
768 *Cell Biol.* *33*, 119–124.
- 769 Hernandez-Gea, V., and Friedman, S.L. (2011). Pathogenesis of liver fibrosis. *Annu. Rev.*  
770 *Pathol.* *6*, 425–56.
- 771 Igal, R.A., Wang, P., and Coleman, R.A. (1997). Triacsin C blocks de novo synthesis of  
772 glycerolipids and cholesterol esters but not recycling of fatty acid into phospholipid:  
773 evidence for functionally separate pools of acyl-CoA. *Biochem. J.* *324*, 529.
- 774 Jiang, W., and Napoli, J.L. (2012). Reorganization of cellular retinol-binding protein type  
775 1 and lecithin:retinol acyltransferase during retinyl ester biosynthesis. *Biochim. Biophys.*  
776 *Acta* *1820*, 859–869.
- 777 Kamentsky, L., Jones, T.R., Fraser, A., Bray, M.-A., Logan, D.J., Madden, K.L., Ljosa,  
778 V., Rueden, C., Eliceiri, K.W., and Carpenter, A.E. (2011). Improved structure, function  
779 and compatibility for CellProfiler: modular high-throughput image analysis software.  
780 *Bioinformatics* *27*, 1179–1180.

- 781 Kassan, A., Herms, A., Fernández-Vidal, A., Bosch, M., Schieber, N.L., Reddy, B.J.N.,  
782 Fajardo, A., Gelabert-Baldrich, M., Tebar, F., Enrich, C., et al. (2013). Acyl-CoA  
783 synthetase 3 promotes lipid droplet biogenesis in ER microdomains. *J. Cell Biol.* *203*,  
784 985–1001.
- 785 Khandelia, H., Duelund, L., Pakkanen, K.I., and Ipsen, J.H. (2010). Triglyceride blisters  
786 in lipid bilayers: implications for lipid droplet biogenesis and the mobile lipid signal in  
787 cancer cell membranes. *PloS One* *5*, e12811.
- 788 Kluwe, J., Wongsiriroj, N., Troeger, J.S., Gwak, G.-Y., Dapito, D.H., Pradere, J.-P., Jiang,  
789 H., Siddiqi, M., Piantedosi, R., O’Byrne, S.M., et al. (2011). Absence of hepatic stellate  
790 cell retinoid lipid droplets does not enhance hepatic fibrosis but decreases hepatic  
791 carcinogenesis. *Gut* 1–10.
- 792 Krahrmer, N., Guo, Y., Wilfling, F., Hilger, M., Lingrell, S., Heger, K., Newman, H.W.,  
793 Schmidt-Supprian, M., Vance, D.E., Mann, M., et al. (2011). Phosphatidylcholine  
794 synthesis for lipid droplet expansion is mediated by localized activation of  
795 CTP:phosphocholine cytidylyltransferase. *Cell Metab.* *14*, 504–15.
- 796 Krahrmer, N., Farese, R.V., and Walther, T.C. (2013). Balancing the fat: lipid droplets and  
797 human disease. *EMBO Mol. Med.* *5*, 973–983.
- 798 Liu, L., and Gudas, L.J. (2005). Disruption of the lecithin:retinol acyltransferase gene  
799 makes mice more susceptible to vitamin A deficiency. *J. Biol. Chem.* *280*, 40226–34.
- 800 MacDonald, P.N., and Ong, D.E. (1988). A lecithin:retinol acyltransferase activity in  
801 human and rat liver. *Biochem. Biophys. Res. Commun.* *156*, 157–63.
- 802 Mardian, E.B., Bradley, R.M., and Duncan, R.E. (2015). The HRASLS (PLA/AT)  
803 subfamily of enzymes. *J. Biomed. Sci.* *22*, 99.
- 804 Marrink, S.J., de Vries, A.H., and Mark, A.E. (2004). Coarse Grained Model for  
805 Semiquantitative Lipid Simulations. *J. Phys. Chem. B* *108*, 750–760.
- 806 Marrink, S.J., Risselada, H.J., Yefimov, S., Tieleman, D.P., and de Vries, A.H. (2007).  
807 The MARTINI force field: coarse grained model for biomolecular simulations. *J. Phys.*  
808 *Chem. B* *111*, 7812–7824.
- 809 Mederacke, I., Hsu, C.C., Troeger, J.S., Huebener, P., Mu, X., Dapito, D.H., Pradere,  
810 J.-P., and Schwabe, R.F. (2013). Fate tracing reveals hepatic stellate cells as dominant  
811 contributors to liver fibrosis independent of its aetiology. *Nat. Commun.* *4*, 2823.
- 812 Moise, A.R., Golczak, M., Imanishi, Y., and Palczewski, K. (2007). Topology and  
813 membrane association of lecithin: retinol acyltransferase. *J. Biol. Chem.* *282*, 2081–90.

- 814 Molenaar, M.R., Vaandrager, A.B., and Helms, J.B. (2017). Some Lipid Droplets Are  
815 More Equal Than Others: Different Metabolic Lipid Droplet Pools in Hepatic Stellate  
816 Cells. *Lipid Insights* 10, 1178635317747281.
- 817 Monticelli, L., Kandasamy, S.K., Periole, X., Larson, R.G., Tieleman, D.P., and Marrink,  
818 S.-J. (2008). The MARTINI Coarse-Grained Force Field: Extension to Proteins. *J. Chem.*  
819 *Theory Comput.* 4, 819–834.
- 820 Mitsche, M.A., and Small, D.M. (2013). Surface pressure-dependent conformation  
821 change of apolipoprotein-derived amphipathic  $\alpha$ -helices. *J. Lipid Res.* 54, 1578–1588.
- 822 O’Byrne, S.M., Wongsiriroj, N., Libien, J., Vogel, S., Goldberg, I.J., Baehr, W.,  
823 Palczewski, K., and Blaner, W.S. (2005). Retinoid absorption and storage is impaired in  
824 mice lacking lecithin:retinol acyltransferase (LRAT). *J. Biol. Chem.* 280, 35647–57.
- 825 Orland, M.D., Anwar, K., Cromley, D., Chu, C.-H., Chen, L., Billheimer, J.T., Hussain,  
826 M.M., and Cheng, D. (2005). Acyl coenzyme A dependent retinol esterification by acyl  
827 coenzyme A: diacylglycerol acyltransferase 1. *Biochim. Biophys. Acta* 1737, 76–82.
- 828 Pol, A., Gross, S.P., and Parton, R.G. (2014). Review: biogenesis of the multifunctional  
829 lipid droplet: lipids, proteins, and sites. *J. Cell Biol.* 204, 635–46.
- 830 Prévost, C., Sharp, M.E., Kory, N., Lin, Q., Voth, G.A., Farese, R.V., and Walther, T.C.  
831 (2018). Mechanism and Determinants of Amphipathic Helix-Containing Protein  
832 Targeting to Lipid Droplets. *Dev. Cell* 44, 73–86.e4.
- 833 Pronk, S., Páll, S., Schulz, R., Larsson, P., Bjelkmar, P., Apostolov, R., Shirts, M.R.,  
834 Smith, J.C., Kasson, P.M., van der Spoel, D., et al. (2013). GROMACS 4.5: a  
835 high-throughput and highly parallel open source molecular simulation toolkit. *Bioinforma.*  
836 *Oxf. Engl.* 29, 845–854.
- 837 Riccalton-Banks, L., Liew, C., Bhandari, R., Fry, J., and Shakesheff, K. (2003).  
838 Long-term culture of functional liver tissue: three-dimensional coculture of primary  
839 hepatocytes and stellate cells. *Tissue Eng.* 9, 401–410.
- 840 Ross, A.C. (1981). Separation of long-chain fatty acid esters of retinol by  
841 high-performance liquid chromatography. *Anal. Biochem.* 115, 324–330.
- 842 Ross, A.C., and Zolfaghari, R. (2004). Regulation of Hepatic Retinol Metabolism:  
843 Perspectives from Studies on Vitamin A Status. *J. Nutr.* 134, 269S–275S.
- 844 Ruiz, A., and Bok, D. (2010). Focus on molecules: lecithin retinol acyltransferase. *Exp.*  
845 *Eye Res.* 90, 186–7.

- 846 Ruiz, a, Winston, A., Lim, Y.H., Gilbert, B.A., Rando, R.R., and Bok, D. (1999).  
847 Molecular and biochemical characterization of lecithin retinol acyltransferase. *J. Biol.*  
848 *Chem.* 274, 3834–41.
- 849 Sandager, L., Gustavsson, M.H., Stahl, U., Dahlqvist, A., Wiberg, E., Banas, A., Lenman,  
850 M., Ronne, H., and Stymne, S. (2002). Storage Lipid Synthesis Is Non-essential in Yeast.  
851 *J. Biol. Chem.* 277, 6478–6482.
- 852 Small, D.M., Wang, L., and Mitsche, M.A. (2009). The adsorption of biological peptides  
853 and proteins at the oil/water interface. A potentially important but largely unexplored  
854 field. *J. Lipid Res.* 50 *Suppl.*, S329-334.
- 855 Spandl, J., White, D.J., Peychl, J., and Thiele, C. (2009). Live cell multicolor imaging of  
856 lipid droplets with a new dye, LD540. *Traffic Cph. Den.* 10, 1579–84.
- 857 Tautenhahn, R., Patti, G.J., Rinehart, D., and Siuzdak, G. (2012). XCMS Online: a  
858 web-based platform to process untargeted metabolomic data. *Anal. Chem.* 84,  
859 5035–5039.
- 860 Testerink, N., Ajat, M., Houweling, M., Brouwers, J.F., Pully, V.V., van Manen, H.J.,  
861 Otto, C., Helms, J.B., and Vaandrager, A.B. (2012). Replacement of retinyl esters by  
862 polyunsaturated triacylglycerol species in lipid droplets of hepatic stellate cells during  
863 activation. *PLoS ONE* 7.
- 864 Thiam, A.R., and Beller, M. (2017). The why, when and how of lipid droplet diversity. *J.*  
865 *Cell Sci.* 130, 315–324.
- 866 Thiam, A.R., and Forêt, L. (2016). The physics of lipid droplet nucleation, growth and  
867 budding. *Biochim. Biophys. Acta* 1861, 715–22.
- 868 Thoen, L.F.R., Guimarães, E.L.M., Dollé, L., Mannaerts, I., Najimi, M., Sokal, E., and  
869 van Grunsven, L. a (2011). A role for autophagy during hepatic stellate cell activation. *J.*  
870 *Hepatol.* 55, 1353–1360.
- 871 Tuohetahuntala, M., Molenaar, M.R., Spee, B., Brouwers, J.F.J.F., Houweling, M.,  
872 Vaandrager, A.B., and Helms, J.B.B. (2016). ATGL and DGAT1 are involved in the  
873 turnover of newly synthesized triacylglycerols in hepatic stellate cells. *J. Lipid Res.* 57,  
874 1162–1174.
- 875 Tuohetahuntala, M., Molenaar, M.R., Spee, B., Brouwers, J.F.J.F., Wubbolts, R.,  
876 Houweling, M., Yan, C., Du, H., VanderVen, B.C.B.C., Vaandrager, A.B., et al. (2017).  
877 Lysosome-mediated degradation of a distinct pool of lipid droplets during hepatic stellate  
878 cell activation. *J. Biol. Chem.* 292, 12436–12448.



- 879 Vamparys, L., Gautier, R., Vanni, S., Bennett, W.F.D., Tieleman, D.P., Antonny, B.,  
880 Etchebest, C., and Fuchs, P.F.J. (2013). Conical lipids in flat bilayers induce packing  
881 defects similar to that induced by positive curvature. *Biophys. J.* *104*, 585–593.
- 882 Walther, T.C., and Farese, R.V. (2012). Lipid droplets and cellular lipid metabolism.  
883 *Annu. Rev. Biochem.* *81*, 687–714.
- 884 Walther, T.C., Chung, J., and Farese, R.V. (2017). Lipid Droplet Biogenesis. *Annu. Rev.*  
885 *Cell Dev. Biol.* *33*, 491–510.
- 886 Wassenaar, T.A., Ingólfsson, H.I., Priess, M., Marrink, S.J., and Schäfer, L.V. (2013).  
887 Mixing MARTINI: electrostatic coupling in hybrid atomistic-coarse-grained  
888 biomolecular simulations. *J. Phys. Chem. B* *117*, 3516–3530.
- 889 Wassenaar, T.A., Pluhackova, K., Moussatova, A., Sengupta, D., Marrink, S.J., Tieleman,  
890 D.P., and Böckmann, R.A. (2015a). High-Throughput Simulations of Dimer and Trimer  
891 Assembly of Membrane Proteins. The DAFT Approach. *J. Chem. Theory Comput.* *11*,  
892 2278–91.
- 893 Wassenaar, T.A., Ingólfsson, H.I., Böckmann, R.A., Tieleman, D.P., and Marrink, S.J.  
894 (2015b). Computational lipidomics with insane: A versatile tool for generating custom  
895 membranes for molecular simulations. *J. Chem. Theory Comput.* *11*, 2144–2155.
- 896 Welte, M.A. (2015). Expanding roles for lipid droplets. *Curr. Biol.* *25*, R470–R481.
- 897
- 898

899 **Tables**

900

901 **Table 1.** Interfacial tension values by drop tensiometry

<b>system</b>	<b>tension (mN/m)</b>
TOG / H <sub>2</sub> O	32
RP <sup>1</sup> / H <sub>2</sub> O	8-14
TOG / DOPC / H <sub>2</sub> O	0.5-0.6
RP <sup>1</sup> / DOPC / H <sub>2</sub> O	0.08-0.2

902 <sup>1</sup>*based on density provided by manufacturer, 0.90-0.95 g/mL*

903

904

## 905 **Figure Legends**

906

907 **Figure 1.** *Lipid droplets containing retinyl esters have a distinct morphology.*

908 **(A)** Chemical structures of the neutral lipids retinyl palmitate, cholesteryl oleate, and  
909 trioleoylglycerol. **(B)** Reaction mechanism of LRAT. **(C,D)** Confocal microscopy of  
910 murine hepatic stellate cells (mHSCs) cultured for 1, 3, 6 or 8 days, stained with DAPI  
911 (blue), LD540 (green) and anti-desmin (red) **(C)**, or DAPI (blue) and anti- $\alpha$ -SMA (red)  
912 **(D)**. Scale bars indicate 50  $\mu$ m. **(E)** Relative expression of LRAT mRNA in mHSCs after  
913 1 or 7 days of culture by qPCR. Barplot indicates means  $\pm$  SEM of 3 animals. Statistical  
914 significance was determined by a two-tailed paired Welch's t-test. **(F)** Confocal  
915 microscopy of mHSCs two hours after isolation, showing UV-autofluorescence (blue),  
916 LD540 (green) and anti-desmin (red). Bottom panel is a zoomed inset of the area  
917 surrounded by dotted lines in the main panel. Closed triangles indicate UV<sup>-</sup> LDs, open  
918 triangles indicate UV<sup>+</sup> LDs. Scale bars indicate 50  $\mu$ m. **(G,H)** Confocal microscopy of  
919 CHO-k1 cells expressing GFP or LRAT-GFP, incubated overnight in the presence or  
920 absence of 20  $\mu$ M ROH or 200  $\mu$ M OA. Imaged channels are DAPI (blue) and LD540  
921 (green) **(G)**, or UV-autofluorescence (left) and LD540 (middle) **(H)**. Scale bars indicate  
922 10 $\mu$ m. **(I)** Full projections of 3D-SIM images of CHO-k1 cells expressing LRAT-GFP,  
923 incubated overnight in the presence 20  $\mu$ M ROH or 200  $\mu$ M OA. Bottom panels are  
924 zoomed insets of areas surrounded by dotted lines in the top panels. Scale bars indicate  
925 10 $\mu$ m. \* P < 0.05, \*\* P < 0.01, \*\*\* P < 0.001, NS: not significant.

926

927

928 **Figure 2.** *LRAT-mediated LD-formation in the absence of pre-existing LDs*

929 **(A)** Confocal microscopy of CHO-k1 expressing LRAT-GFP. After pre-incubation with  
930 medium containing 1% FBS, cells were incubated overnight with or without 200  $\mu$ M OA  
931 or 20  $\mu$ M ROH, in the presence or absence of 1  $\mu$ g/mL triacsin C. Cells were stained with  
932 DAPI (blue) and LD540 (green). Scale bars indicate 10  $\mu$ m. **(B)** Quantification of  
933 predominant RE-species by LC-MS/MS of wt and 4 $\Delta$  yeast cells expressing LRAT, 2  
934 hours after incubation in the presence or absence of 2 mM ROH. Amounts in pmol RE  
935 per  $\mu$ g protein. Barplot indicates means  $\pm$  SD. **(C)** Wide-field microscopy of  
936 Erg6-mCherry expressing wt and 4 $\Delta$  yeast cells, with or without expressing LRAT, 2  
937 hours after incubation with or without 2 mM ROH ('-' or '+'). Images of  
938 UV-autofluorescence (green), Erg6-mCherry (red) and brightfield were taken. Scale bars  
939 indicate 5  $\mu$ m. **(D)** Electron microscopy of wt and 4 $\Delta$  yeast cells, with or without  
940 expressing LRAT, incubated with or without 2 mM ROH. ER, endoplasmic reticulum;  
941 LD, lipid droplet; M, mitochondria; N, nucleus. Scale bars indicate 250 nm.

942

943 *(Cont. Fig. 2)* **(E)** Electron microscopy of yft2 $\Delta$ scs3 $\Delta$ , and 4 $\Delta$  yeast cells expressing  
944 LRAT, incubated with 2 mM ROH. Scale bars indicate 100 nm. ER, endoplasmic  
945 reticulum (yellow lines in right panels); LD, lipid droplet (red lines right panels). **(F)**  
946 Wide-field microscopy of Erg6-mCherry expressing wt yeast cells expressing LRAT. Two  
947 time series of UV-autofluorescence (white), Erg6-mCherry (red) and brightfield, taken 2,  
948 4, 6 and 8 minutes after addition of 2 mM ROH. Scale bars indicate 5  $\mu$ m.

949

950

951 **Figure 3. Nucleation and budding properties of RE.**  
952 **(A,B)** Coarse grain MD simulations of lens formation by 150 (18%) (A) and 250 (30%)  
953 (B) neutral lipids per leaflet in a POPC membrane. Colors indicate the neutral lipid  
954 composition, with marine for pure RE and red for pure TOG. The progress of lens  
955 formation is shown as fractional loss of interactions between the neutral lipids and POPC  
956 as function of time (log-scale). **(C)** Brightfield microscopy images of droplet interface  
957 bilayers of droplets containing neutral lipid RP and lipid surfactants PC, PE or PA. Scale  
958 bars indicate 20  $\mu\text{m}$ . **(D)** Comparison of quantified budding angles (mean $\pm$ SD) of  
959 RP-containing droplets with lipid surfactants PC (176,2 $\pm$ 2,8), PE (150,9 $\pm$ 4,0) or PA  
960 (129,5 $\pm$ 5,7) vs. reported budding angles of TAG and SQ-containing droplets (Ben  
961 M'barek et al., 2017). Barplot represent means of at least 8 individual measurements,  
962 which are shown as black dots.

963  
964 **Figure 4. Deletion of N-terminus of LRAT affects LD formation in CHO cells.**  
965 **(A,B)** *In vitro* LRAT-activity of CHO-k1 homogenates expressing full-length or  
966  $\Delta\text{Nt}$ -LRAT-GFP. After incubation full-length LRAT-GFP with PC(7:0/7:0) and varying  
967 concentration of ROH, ROH (peak a), RE(2:0) (internal standard, peak b) and RE(7:0)  
968 (peak c) were measured by LC-MS/MS. MRM-transition 269/93 detects all retinoid  
969 backbones (blue), whereas 399/269 specifically detects RE(7:0) (red) **(A)**.  
970 RE(7:0)-synthesis by full-length or  $\Delta\text{Nt}$ -LRAT-GFP was normalized by GFP-levels of the  
971 homogenates and plotted against increasing ROH concentrations. Estimated Km values  
972 are indicated by vertical dashed lines. A representative plot of three independent  
973 experiment is shown **(B)**. **(C,D)** Confocal microscopy of CHO-k1 cells expressing  
974 LRAT-GFP or  $\Delta\text{Nt}$ -LRAT-GFP, incubated overnight in the presence or absence of 20  $\mu\text{M}$   
975 ROH. Imaged channels are DAPI (blue) and LD540 (green) **(C)**, or UV-autofluorescence  
976 (top) and LD540 (middle) **(D)**. Scale bars indicate 10  $\mu\text{m}$ . **(E,F)** Quantification of cells  
977 imaged by confocal microscopy. Cell sizes were plotted against total LD volume per cell  
978 (LRAT-GFP or  $\Delta\text{Nt}$ -LRAT-GFP) and cells with similar total LD volumes per cell were  
979 gated (black box, LRAT-GFP+OA: 12 cells;  $\Delta\text{Nt}$ -LRAT-GFP+OA: 40 cells;  
980 LRAT-GFP+ROH: 13 cells;  $\Delta\text{Nt}$ -LRAT-GFP+ROH: 31 cells) **(E)**. The gated cells were  
981 expressed as log-ratios of mean LD volume vs. LD number. Mean values ( $\pm$ SD) were  
982 -1,96 $\pm$ 1,34 (LRAT-GFP with OA); -1,83 $\pm$ 1,06 ( $\Delta\text{Nt}$ -LRAT-GFP with OA); -0,68 $\pm$ 1,51  
983 (LRAT-GFP with ROH); and -1,55 $\pm$ 1,08 ( $\Delta\text{Nt}$ -LRAT-GFP with ROH) Statistical  
984 significance was determined by two-tailed unpaired Student's t-tests, P-values were  
985 corrected by the Benjamini-Hochberg procedure **(F)**. Cells were incubated overnight with  
986 200  $\mu\text{M}$  OA (red circles) or 20  $\mu\text{M}$  ROH (blue circles) and LD number per cell as a  
987 function of total LD volume per cell for LRAT-GFP (closed circles) or  
988  $\Delta\text{Nt}$ -LRAT-GFP-expressing (open circles) was analyzed without gating **(G)**. Every data  
989 point represents one cell. Lines are moving averages, shades indicate 95% confidence  
990 intervals. LRAT-GFP+OA: 35 cells;  $\Delta\text{Nt}$ -LRAT-GFP+OA: 79 cells; LRAT-GFP+ROH:  
991 43 cells;  $\Delta\text{Nt}$ -LRAT-GFP+ROH: 68 cells. \* P < 0.05, \*\* P < 0.01, \*\*\* P < 0.001, NS: not  
992 significant.  
993

994 **Figure 5. Amphipathic properties of LRAT-Nt and CCT- $\alpha$  P2 helices.**  
995 **(A)** Helical wheel projections by HeliQuest of LRAT-Nt (top) and CCT- $\alpha$  P2 (bottom).  
996 Colors indicate amino acid categories: hydrophobic (yellow), negatively charged (red),  
997 polar (purple), positively charged (blue) and other (gray) residues. The hydrophobic  
998 moment is indicated with a black arrow. **(B)** Peptide-membrane interaction energies for  
999 LRAT-Nt (top) and CCT- $\alpha$  P2 with pure POPC (red) and with an 85:15 POPC/DOG  
1000 mixture (red) over time across DAFT simulation ensembles of 30 simulations each,  
1001 showing the region from the 1st to 3rd quartile as shaded areas and the median interaction  
1002 energy for each ensemble of simulations as solid line. **(C)** Insertion depth of LRAT-Nt  
1003 and CCT- $\alpha$  P2, showing the helical wheels of LRAT-Nt (top) and CCT- $\alpha$  P2 according to  
1004 their mean angular orientations, with a red line signifying the position of the helix center,  
1005 the thick black line denoting the median position of the lipid head groups across  
1006 simulations and the thinner line denoting the standard deviation of the median across  
1007 simulations. Colors in the peptides are as described in panel A.

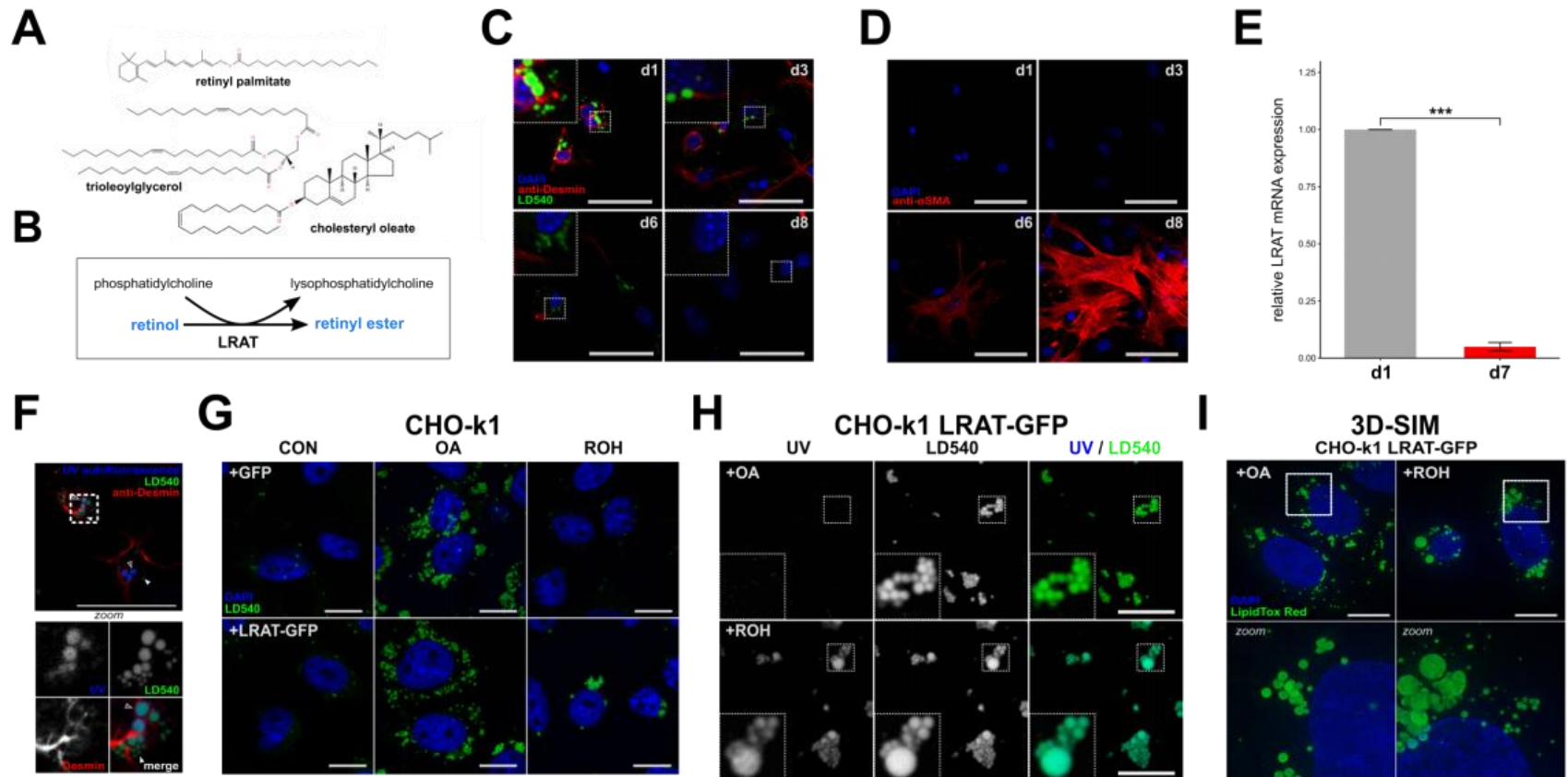
1008  
1009 **Figure 6. Affinity of LRAT-Nt for retinyl esters in GC-MD.**  
1010 **(A)** Binding of LRAT-Nt to lenses consisting of 300 molecules RP (left), 120+180  
1011 molecules RP+TOG (middle) and 300 molecules TOG (right). The panels show  
1012 preferential binding of the helix (green) to the region of maximal curvature. The RP and  
1013 TOG particles are shown in marine and red, respectively. **(B)** Positions of centers of mass  
1014 of LRAT-Nt with respect to the membrane as function of the ratio RP:TOG (marine: pure  
1015 RP to red: pure TOG). The membrane is shown as density profile, while the positions of  
1016 LRAT-Nt are marked with dashed lines. **(C)** Specificity of interaction of LRAT-Nt with  
1017 RP over TOG. Each simulation represents a dot and indicates the interaction energy  
1018 between LRAT-Nt and RP on the x-axis and between LRAT-Nt and TOG on the y-axis.  
1019 Dot size reflects the total number of neutral lipids and the color signifies the ratio  
1020 between RP and TOG as indicated. The dashed line has slope -1 and a parallel profile is  
1021 indicative of a transition from one pure compound to the other with no preferential  
1022 interactions. The observations show a lower interaction with TOG as compared to RP,  
1023 resulting in a profile with a reduced slope.

1024  
1025 **Figure 7. LRAT N-terminal peptide shows strong association with retinyl palmitate**  
1026 **droplets.** **(A)** Left, peptide addition to the buffer surrounding a pending oil droplet,  
1027 trioleoylglycerol (TOG) or retinyl palmitate (RP), results in a decrease of the interface  
1028 surface tension induced by peptide recruitment. **(B)** Related surface tension quantification  
1029 over time for TOG and RP oil droplets. Arrows indicate time of LRAT-Nt peptide  
1030 injection in the buffer. **(C)** After, equilibrium is reached, the surface of the TOG-droplet  
1031 covered by the peptide is compressed, provoking a drop of surface tension. When  
1032 compression was stopped, surface tension re-increased, indicating desorption of the  
1033 LRAT-Nt peptide from the TOG-buffer interface. Right panel illustrates the manipulations  
1034 and consequence on tension and peptide behavior. **(D)** After the LRAT-Nt peptide was  
1035 recruited to the RP-droplet surface, the interface was compressed, provoking a surface  
1036 tension drop. When compression was stopped, surface tension remained constant,  
1037 indicating a strong association of the peptide with the RP-buffer interface. Right panel  
1038 illustrates the manipulations and consequence on tension and peptide behavior.

1039  
1040

1041 **Figures**

1042



1043

1044

1045

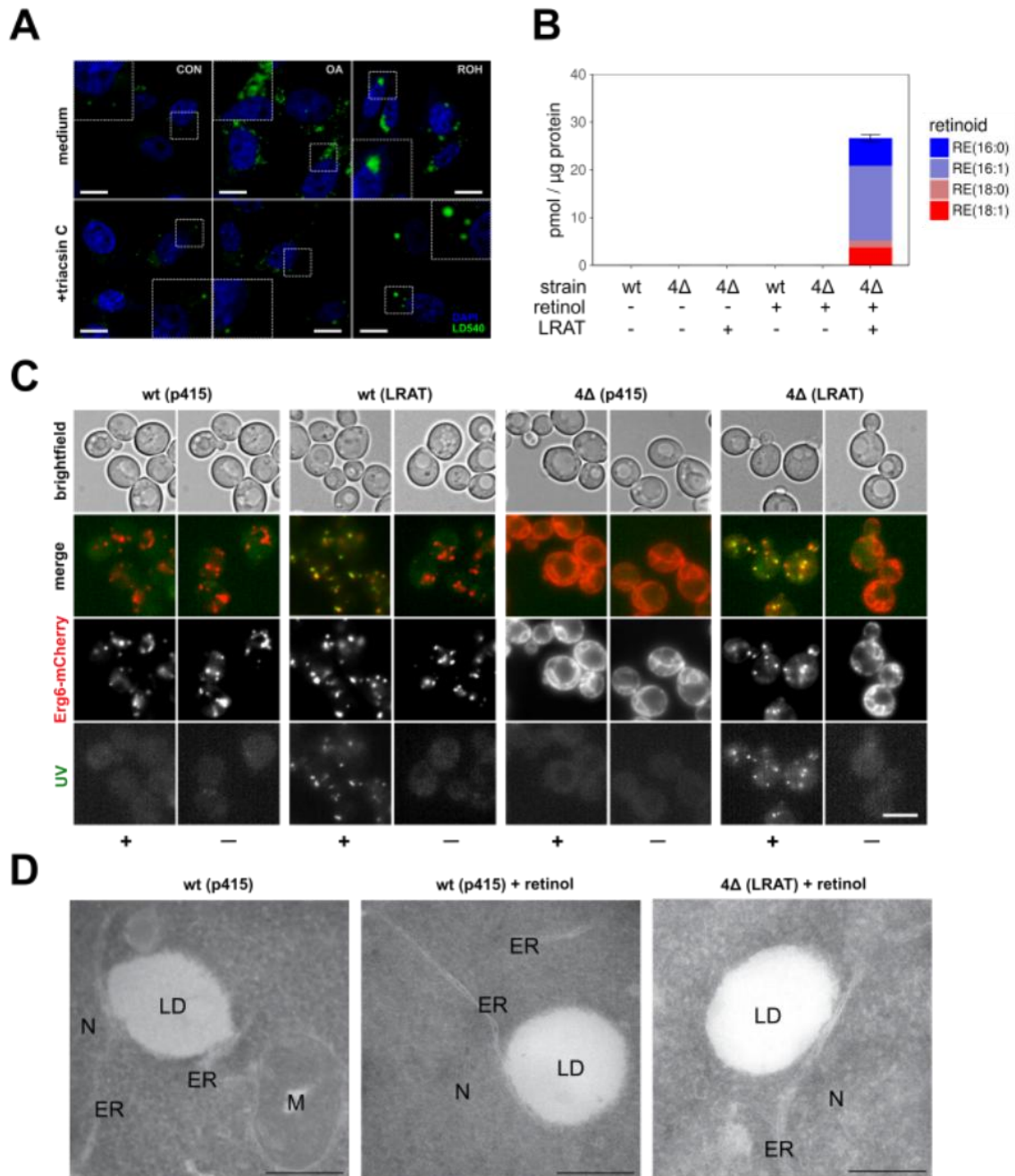
1046

1047

1048

**Figure 1** Molenaar et al

1049



1050

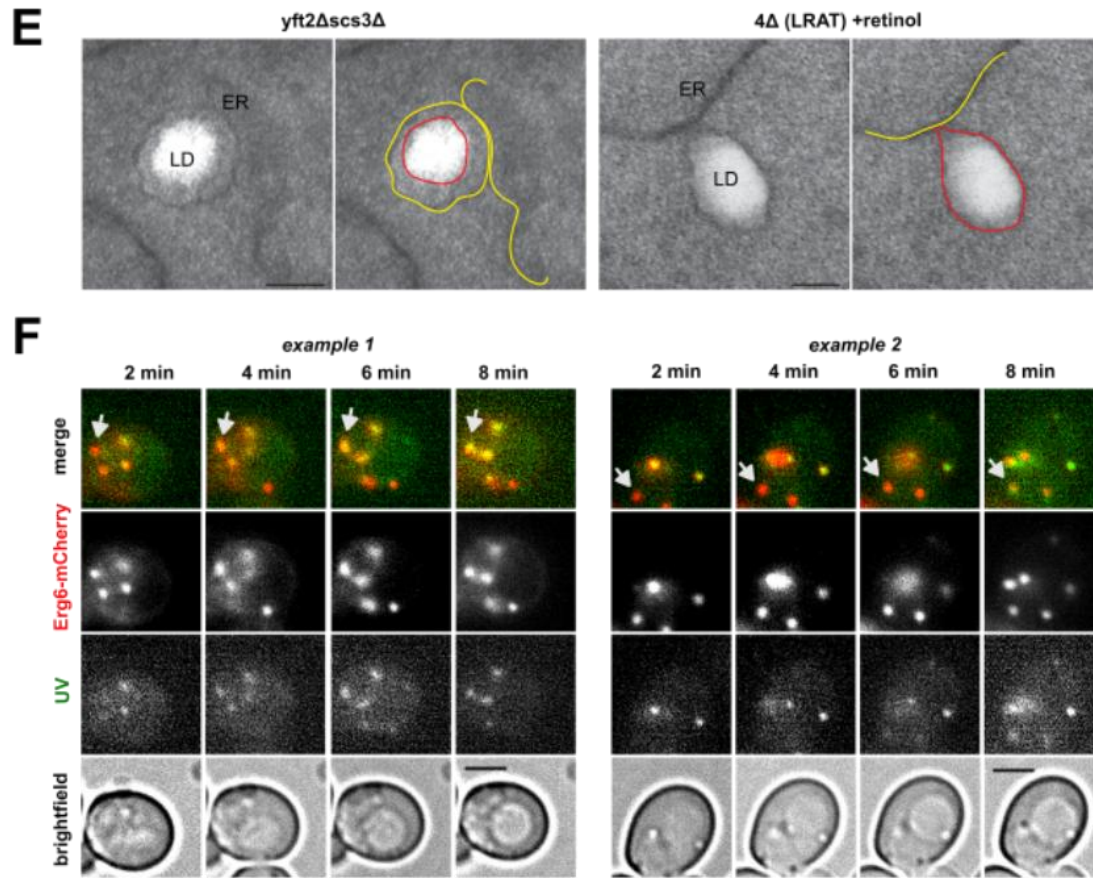
1051

1052

1053

1054 **Figure 2 Molenaar et al**





1055

1056

1057

1058

1059

1060

1061

1062

1063

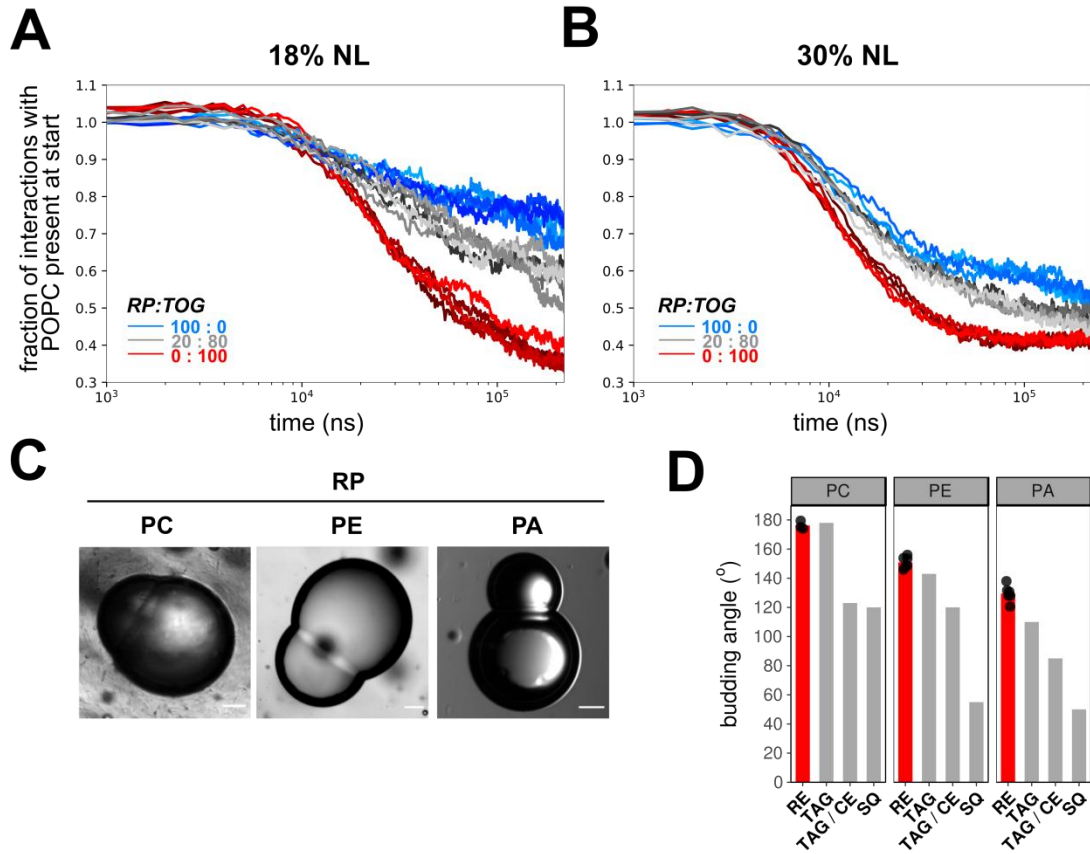
1064

1065

1066

1067

1068 **Figure 2 (cont.) Molenaar et al**



1069

1070

1071

1072

1073

1074

1075

1076

1077

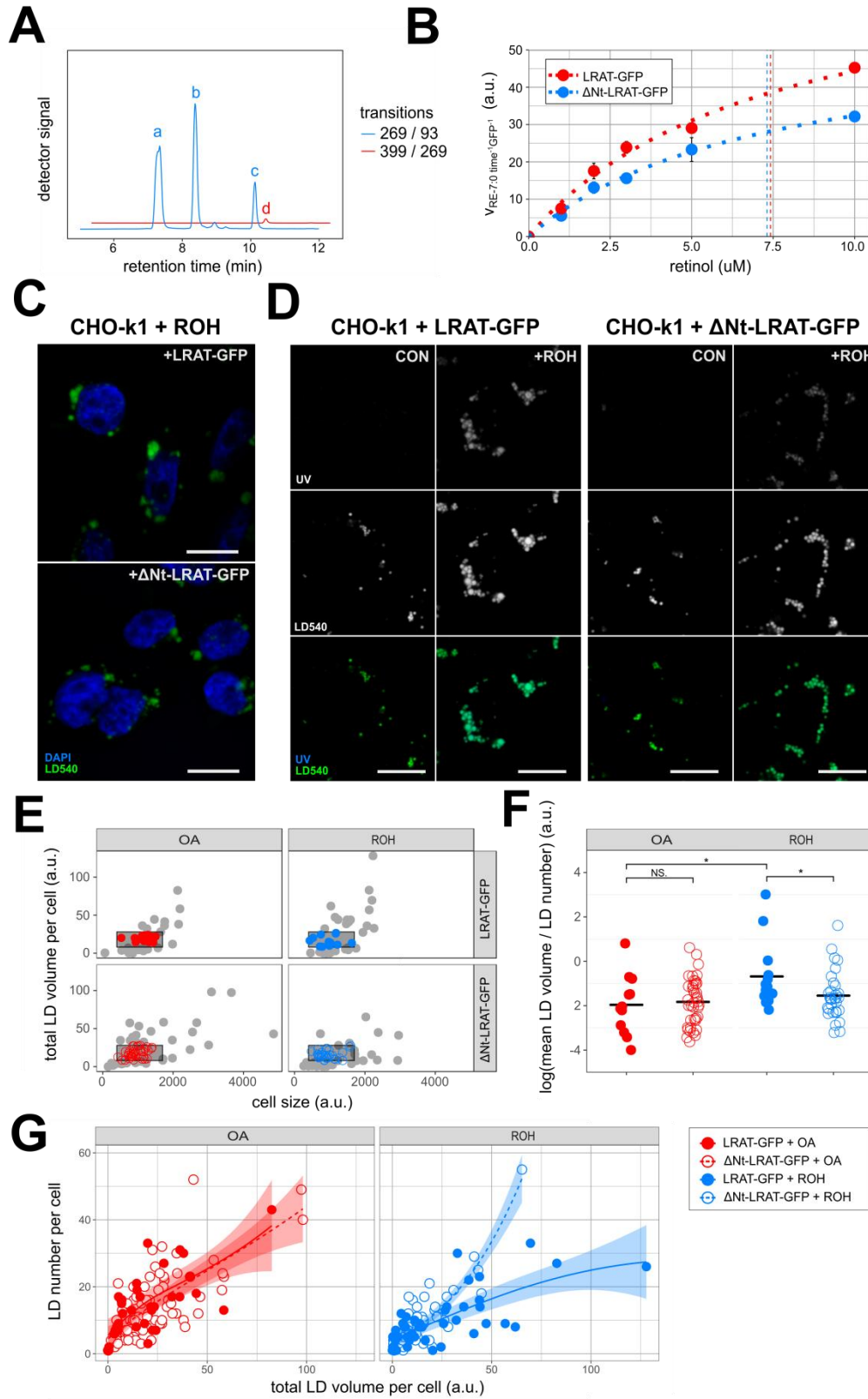
1078

1079

1080

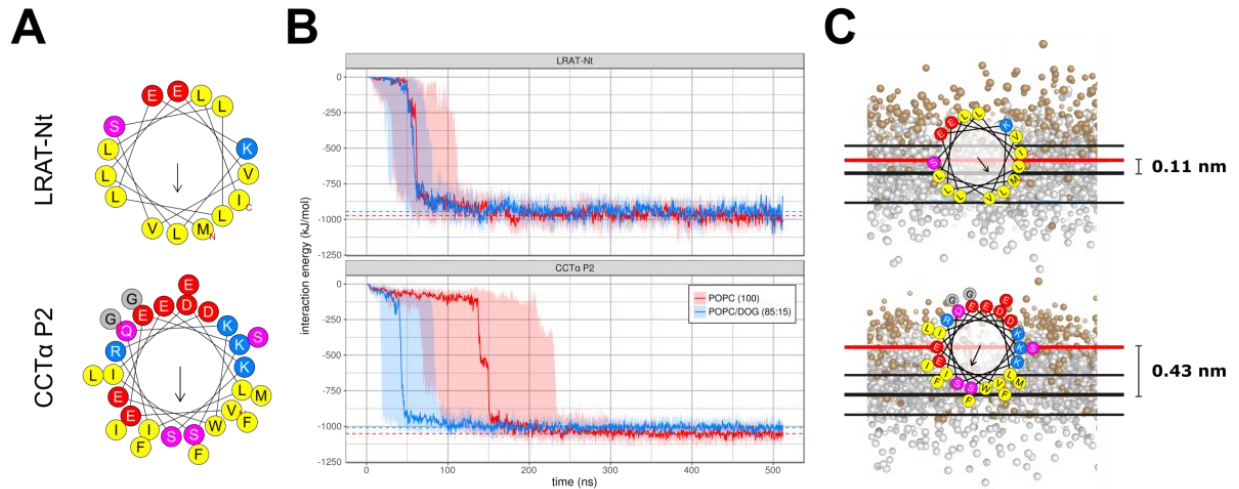
1081

1082 **Figure 3 Molenaar et al**



1083

1084 **Figure 4 Molenaar et al**



1085

1086

1087

1088

1089

1090

1091

1092

1093

1094

1095

1096

1097

1098

1099

1100

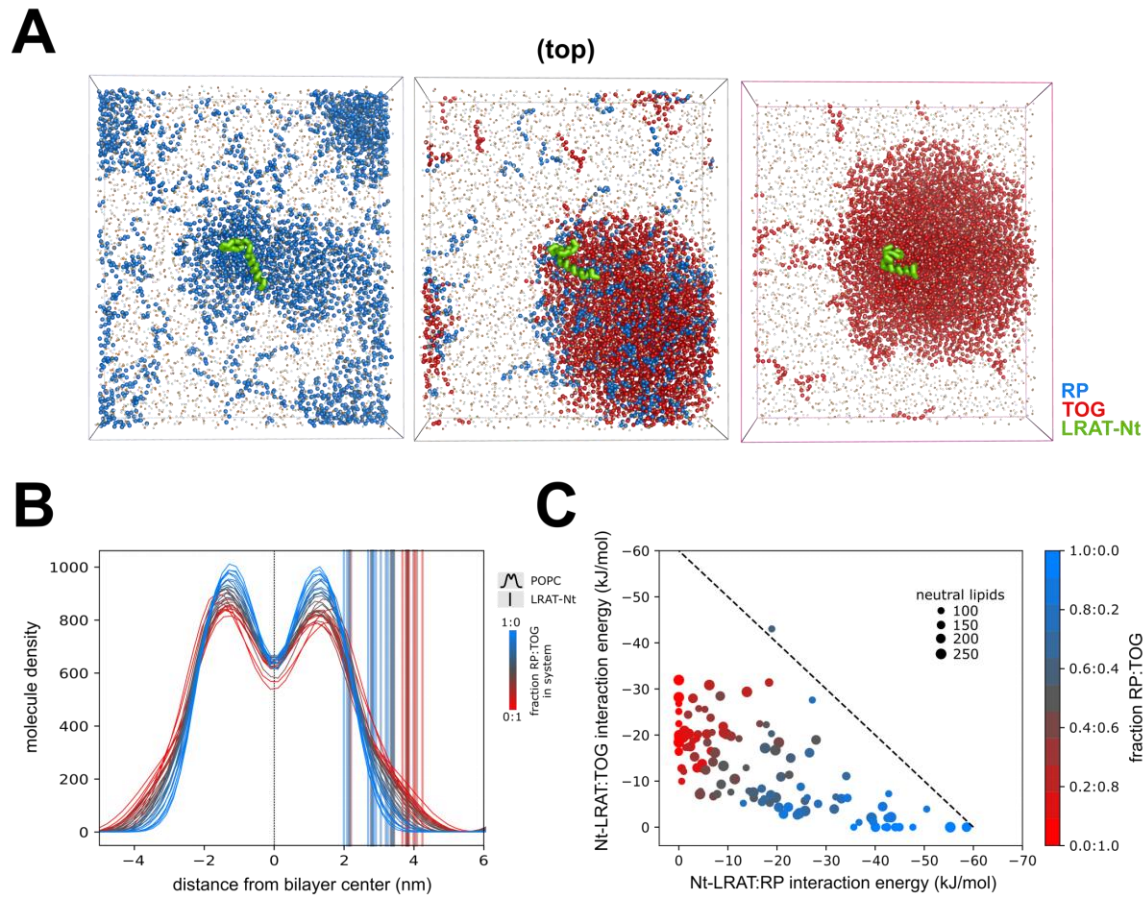
1101

1102

1103

1104

1105 **Figure 5 Molenaar et al**



1106

1107

1108

1109

1110

1111

1112

1113

1114

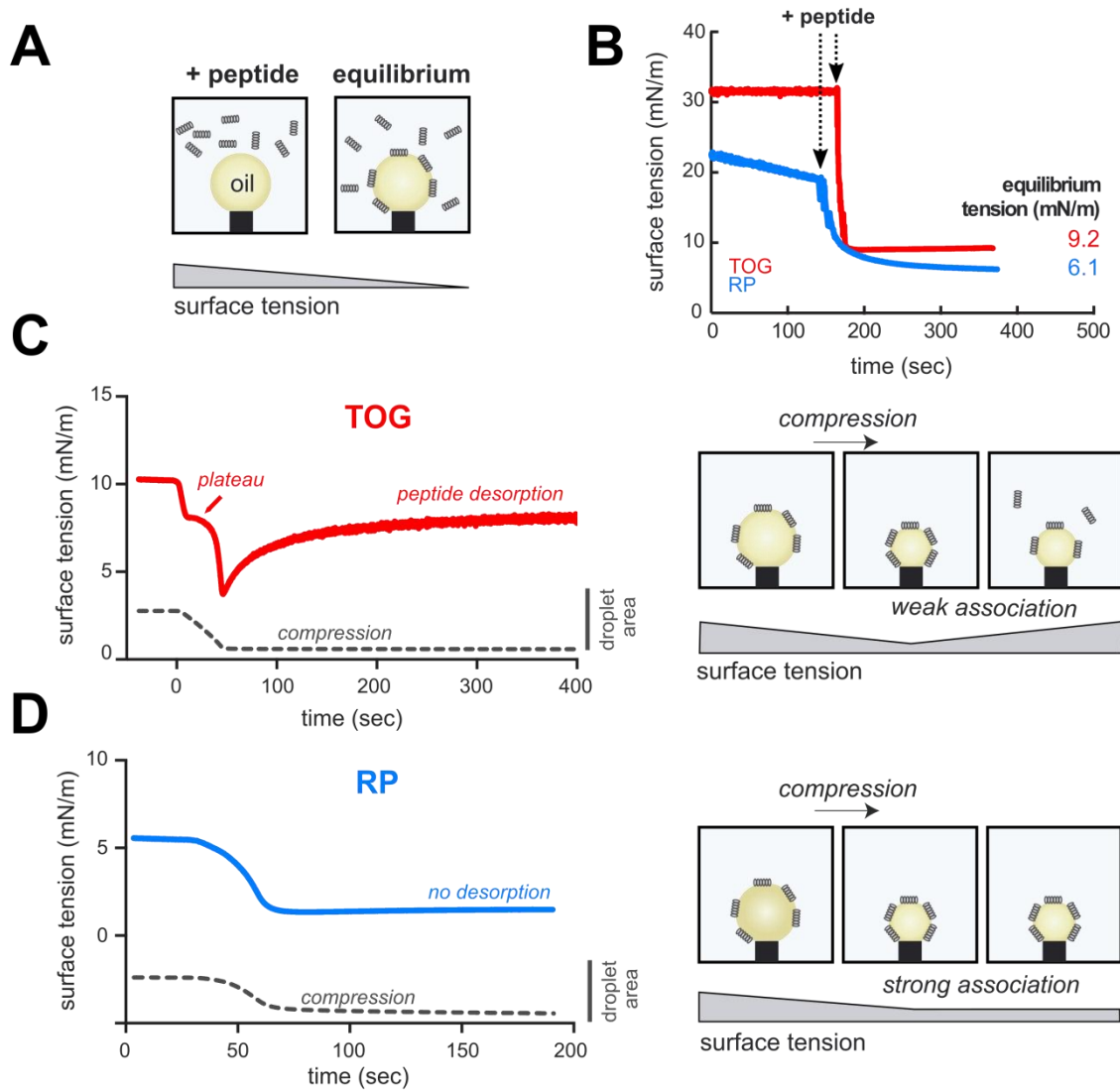
1115

1116

1117

1118

1119 **Figure 6 Molenaar et al**



1120

1121

1122

1123

1124

1125

1126

1127

1128

1129 **Figure 7 Molenaar et al**